UNIVERSITY OF TURKU

Durable Copper Nanowires for Flexible Electronics

Materials Engineering in Health Technology
Department of Mechanical and Materials Engineering
Faculty of Technology
Master's thesis

Author:
Linda Broere

14.04.2026
Turku

UNIVERSITY OF TURKU

Department of Mechanical and Materials Engineering

Master's thesis

Subject: Materials Engineering

Author: Linda Broere

Title: Durable Copper Nanowires for Flexible Electronics

Supervisors: Prof. Vipul Sharma and Dr. Rituporn Gogoi

Number of pages: 61

Date: 14.04.2026

A novel method for developing flexible electronics is to embed conductive metal nanowires (MNWs) onto flexible substrates. Currently, silver nanowires (AgNWs) are one of the most common nanometal inserts in flexible electronic devices. Copper nanowires (CuNWs) have gained significant attention in recent years as an alternative material for flexible electronics. As silver is an expensive material, the use of copper nanowires instead is a much more sustainable and cost-effective solution. In this thesis, ultra-long CuNWs were synthesised in a water/glycerol co-solvent. CuNWs were synthesised at temperatures of 120, 140, 160, and 180 °C, with CuNWs prepared at 160 °C showing the best properties. The CuNW length/diameter ratios were 558, 1356, 1939, and 865, for CuNW-120, CuNW-140, CuNW-160, and CuNW-180, respectively. After depositing the CuNWs onto a polycarbonate (PC) film, thus forming a conductive film, we discovered that the CuNW-160-PC films can maintain stable conductivity over 60 days and have thermal stability up to 140 °C. A capacitive curvature sensor was fabricated using a flexible conductive surface (FCS) with CuNW-160 on the surface of nylon-6 (N-6) nanofibres, which maintained consistent performance over 10,000 bending cycles and exhibited good curvature sensitivity even after 75 days. The excellent performance of the CuNW-160-based FCS proves that CuNWs have the potential to replace AgNWs in flexible electronics, highlighting the potential of enhancing copper nanowire stability by tuning reaction temperature.

Keywords: copper nanowires, flexible electronics, durable sensors

Table of contents

UNIVERSITY
OF TURKU

1 Abbreviations

Term	Meaning
AgNW	Silver nanowire
Au	Gold
AuNW	Gold nanowire
BSE	Back-scattered electron
C	Carbon
CCD	Charge coupled device
Cl	Chlorine
CS	Conductive surface
Cu	Copper
CuNW	Copper nanowire
EDA	Ethylenediamine
EDS	Energy dispersive X-ray spectroscopy
FCE	Flexible conductive electrode
FCS	Flexible conductive surface
FE	Field emission
HR	High resolution
ICDD	International Centre for Diffraction Data
ICP	Intrinsically conductive polymer
LCR	Inductance (L), capacitance (C), and resistance (R)
MNP	Metal nanoparticle
MNW	Metal nanowire
N	Nitrogen
N-6	Nylon-6
NW	Nanowire
O	Oxygen
OA	Oleic acid
ODA	Octadecylamine
OLA	Oleylamine
RH	Relative humidity
RO	Reverse osmosis
PC	Polycarbonate
PES	Polyester
PET	Polyethyelene terephthalate
PtNW	Platinum nanowire
SAED	Selected area electron diffraction

SE	Secondary electron
SEM	Scanning electron microscope / microscopy
TCF	Transparent conductive film
TEM	Transmission electron microscope / microscopy
XPS	X-ray photoelectron spectroscopy
XRD	X-ray diffraction

2 Introduction

The demand for flexible electronics has surged significantly due to their ability to adapt seamlessly to curved surfaces, making them ideal for applications such as wearable sensors [1–3], smart textiles [4,5] and smart medical devices [2]. Research and development in this field are abundant, with publications on flexible wearable electronics increasing exponentially since 2012 [1].

Flexible electronic devices can transform physical forces like pressure, deformation, or bending into measurable electrical signals [6]. This ability to convert physical deformation into electrical responses is a valuable property for next-generation sensing systems, particularly in applications requiring lightweight design and real-time responsiveness. For example, on-skin sensors can monitor physical activity and various medical and biological signals [1]. As the average lifespan increases, there is an increasing demand for continuous medical monitoring of the elderly. In addition, wearable sensors offer maximum comfort for everyday use due to their skin-conforming surfaces. Wearable sensors are typically based on flexible deformable conductive surfaces (FCS) [7].

2.1 Various conductive materials used for flexible electronics

Over the last decade, multiple avenues have been explored in flexible electronics materials research, particularly with respect to the flexible conductive materials required in device fabrication. Research on how well different classes of conductive materials can maintain high electrical performance under mechanical deformation is of key importance for this purpose.

Carbon-based materials are one of the most researched groups of such conductive materials. In particular, carbon nanomaterials have high potential due to their high conductivity and exceptional electron transport properties [7]. Carbon nanotubes (CNTs) and different forms of graphene are some of the carbon-based nanomaterials with the most potential for use in flexible electronics [8]. In addition to their high conductivity, both CNTs and graphene sheets have the potential to exhibit high mechanical flexibility [8]. Although both high conductivity and durability have been achieved with carbon-based conductive materials [7], the conductivities of CNTs and graphene are highly dependent on the quality of the material and how they are fabricated [9]. The performance of CNTs in flexible electronics depends on properties such as length, diameter, chirality, and atomic structures, which have proved difficult to control [7]. Pristine graphene of the correct composition and size is also exceedingly difficult to synthesise [10].

Intrinsically conductive polymer (ICP) films with high conductivity can be directly used as flexible electrodes, without any need for a conductive insert [12]. ICPs are often carbon-based, with examples including polyacetylene, polyaniline and poly(3,4-ethylenedioxythiophene) [12]. They can also be composed of multiple materials, such as in the case of the cellulose film and CNT-based ICP created by Yang et al. [12]. Therefore, ICPs are typically low-cost and have good biocompatibility. Lack of control over the final conducting polymer's microstructure and functionalities, such as conductivity, remains a key issue in the application of ICPs in flexible electronics [13]. The long-term stability of ICP conductivity and mechanical flexibility in severe conditions such as high humidity and high temperature is also challenging to achieve [14]. For example, under high humidity, the conductivity of ICPs can exhibit significant degradation due to oxidation and environmental contamination. To enhance the conductivity of ICP films, metal nanoparticles and nanowires are often used as inserts in conductive polymer-based devices to enhance conductivity [15,16].

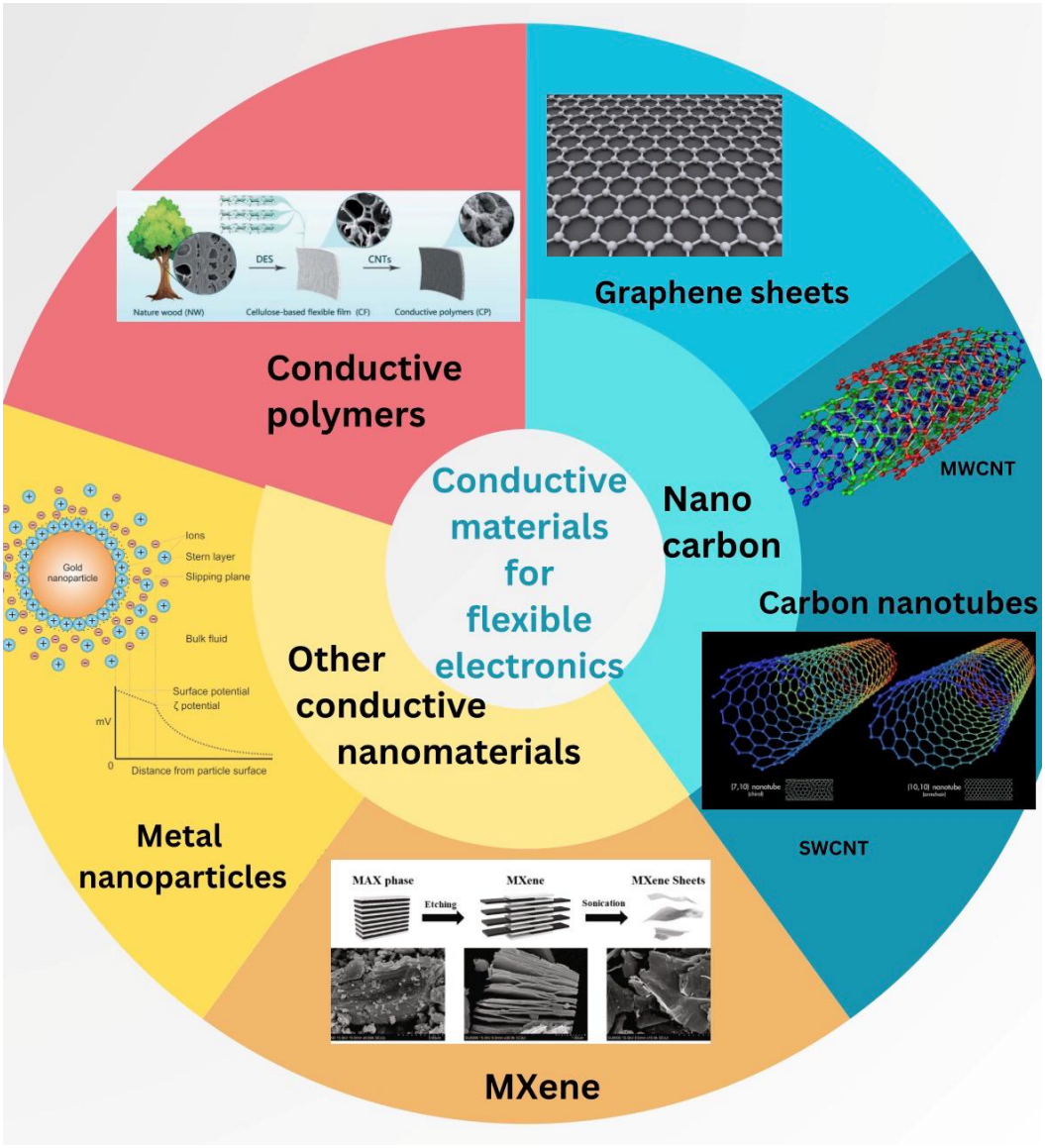

Scheme 1: Conductive materials for flexible electronics. Schematic created by the author and assembled from multiple sources. MWCNTs (Eric Wieser), SWCNTs (User Mstroeck on en.wikipedia), graphene (AlexanderAlUS) and gold nanoparticle (Larryisgood) images reproduced from Wikimedia Commons under the CC BY-SA 3.0 licence. MXene image reproduced from S. K. Hwang et al., *MXene: An emerging two-dimensional layered material for removal of radioactive pollutants*, Elsevier, 2020. [17] Reproduced with permission from Elsevier. Conductive polymer scheme adapted from [12] using CC BY-SA 3.0 licence.

MXenes are a novel family of 2D nanomaterials with exceptional electrical, mechanical and chemical properties. The electrical properties of MXenes are determined by their composition and type of surface end groups [10]. However, MXenes have a complex synthesis process, which is challenging to optimise [18].

Metal nanoparticles (MNPs) and conductive inks prepared from MNPs are another extensively studied area. MNP inks are highly conductive due to the excellent conductivity of the MNPs

themselves as well as their high dispersion stability [19]. The most promising MNP conductive inks for flexible electronics applications are based on gold, silver, and copper nanoparticles [11].

2.2 Metal nanowires for flexible electronics

Metal nanowire (MNW)-based conductive networks have appeared as a promising class of materials. They are especially promising owing to their unique properties, such as high aspect ratios, superior conductivity, and excellent mechanical flexibility [20]. MNWs are a more recent addition to the field of flexible electronics, with the first silver nanowire (AgNW)-based transparent conductive films (TCF) fabricated in 2008 [13]. MNWs can be synthesised easily using wet chemical synthesis protocols, which places them in a better position for application than CNTs, graphene and MXenes.

Silver nanowires (AgNWs) have traditionally dominated this field due to their outstanding electrical conductivity and well-established synthesis methods [18,19]. However, their widespread use is hindered by their high cost and limited availability, driving research toward more sustainable alternatives [21]. Noble metal nanowires, such as gold nanowires (AuNWs) and platinum nanowires (PtNWs), have also been researched for use in flexible electronics [23]. AuNWs have good chemical stability, are easily dispersible in solution, and have excellent electrical and optical properties when integrated into films [24]. However, despite exhibiting superior conductivity and transmittance, both gold and platinum are even more expensive and rare than silver and thus cannot be considered sustainable options for low-cost flexible conductors [24].

Multiple other types of metal nanowires have been researched, which have shown potential to replace AgNWs in flexible electronics. Examples of these include copper [3,4,21] nickel [25–27] and aluminium nanowires, each with their own unique advantages.

Aspect ratio is a critical parameter in determining the performance of MNWs, which influences both the conductivity and transparency of the resulting electrode [28]. Higher aspect ratios (longer nanowires with smaller diameters) lead to enhanced electrical conductivity, as longer nanowires form more interconnected networks, thereby minimising junction resistance [2]. Simultaneously, thinner nanowires contribute to higher optical transparency because they allow more light to pass through the network.

2.3 Why copper nanowires for flexible electronics

Copper nanowires (CuNWs) have gained significant attention in recent years as an alternative material for flexible conductive electrodes (FCEs) [28]. CuNWs stand out due to their exceptionally

high conductivity along with their low price and high abundance, making them one of the most viable sustainable alternatives to AgNWs (**Table 1**) [29,30]. Nevertheless, due to their rapid oxidation in ambient conditions [31], their mechanical and chemical stability is compromised, which significantly limits their durability in practical applications. At present, there are no commercially available CuNW alternatives to AgNWs on the market.

Table 1: Silver vs. copper properties comparison table

Silver	Copper
Much more expensive than copper	~91% less expensive than silver [30]
1000 times less naturally abundant than copper	1000 times more naturally abundant than silver [30]
~6% more conductive than copper	~94% as conductive as silver [29]
More stable to oxidation than copper	Faster aerobic oxidation than silver [29]

To address these limitations, research has focused on enhancing the durability of CuNWs and optimising their structural and chemical properties. The strategies reported in recent literature can be split into synthesis-related, surface treatment and surface protection methods. Nanowire synthesis can be optimised to provide fast and reproducible results [32], ultra-long high-aspect ratio CuNWs [30] and nanowires with durability enhanced by a capping agent [31]. Eliminating nanoparticle by-products after synthesis [33,34] and strategies to increase NW dispersibility [35] can also improve NW properties, such as their chemical stability and conductivity. Common surface treatment related strategies include surface passivation [36] and doping [37], which involve adding another material onto the nanowire surface to enhance their stability. The treatment of CuNW surfaces using acid solutions to cleanse residual oxides is also well-studied [38]. Nanowire networks can also be encapsulated within electrode materials to prevent oxidation [39,40].

The primary challenge in optimising CuNWs for application in flexible electronics lies in the control of their aspect ratio (length-to-diameter ratio), morphology, and uniformity, as these factors strongly influence their electrical and mechanical properties. As mentioned before, higher aspect ratio correlates with the better electrical performance of MNWs as well as the transparency of the resulting electrode [28].

Recent research has focused on achieving ultra-long CuNWs with high aspect ratios [28,38,41]. The challenge lies in maintaining a high aspect ratio while also ensuring chemical stability. Recent advancements highlight the importance of controlling reaction parameters, such as temperature, to

improve the mechanical and chemical stability of single nanowires [2]. Although the synthesis temperature dependence of CuNWs has been studied previously [41,42], its effect on the flexibility and durability of CuNW-based surfaces remains unstudied.

2.4 Aim and objective

This thesis aims to determine if changing the reaction temperature would improve the properties of CuNWs, with the goal of achieving results comparable to those of AgNWs. In our study on this topic [30], we investigated the research gap in the study of the effect of reaction temperature on CuNW properties by focusing on controlling the hydrothermal synthesis temperature, specifically using temperatures of 120 °C, 140 °C, 160 °C and 180 °C. We adapted the synthesis method from literature [28] with the primary objective being to prepare and characterise the nanowires, followed by various tests to evaluate their durability. After these tests, CuNW-based sensors were fabricated, and their device performance and stability were evaluated.

Based on our results, we have proved that the CuNWs prepared at 160 °C have superior qualities to the NWs prepared at other temperatures, having fabricated films and sensors with high conductivity and stability [30]. However, films prepared from all the nanowires proved to have good flexibility and durability under mechanical stress. These results address a critical barrier to the adoption of CuNWs in flexible electronic devices, their low stability due to rapid oxidation [2]. By advancing the understanding and fabrication of copper nanowires, this study contributes to the development of sustainable, high-performance materials for the next generation of flexible electronics.

3 Experimental

3.1 Synthesis of Copper Nanowires

There are two main methods for metallic nanowire (MNW) synthesis - top-down and bottom-up methods. The bottom-up approach using a simple wet-chemical synthesis method has been demonstrated to be one of the most successful routes to control the yield, size, and morphology of the nanowires [9]. Hydrothermal synthesis methods have emerged as one of the most optimal ways for the large-scale fabrication of CuNWs with desirable properties, as they offer additional control over the nucleation and growth mechanisms of the nanowires [43]. Recent studies have determined that linear alkylamines (e.g. octadecylamine (ODA) [34], oleylamine (OLA) [28], ethylenediamine (EDA) [44]) are good capping agents for manipulating the growth of copper nanocrystals into nanowires [2]. Another area of emphasis in research is on developing synthesis protocols using less toxic, biological reducing agents such as glucose [28] or ascorbic acid [42].

This thesis work expands on the reporting done in our article [30], where CuNWs were synthesised based on previous literature with small changes [28]. To begin with, the copper salt $CuCl_2.2H_2O$ (3.35 mmol, 0.6 g) and the reducing agent glucose (4.44 mmol, 0.8 g) were dissolved in 40 mL of reverse-osmosis water in a Teflon-lined autoclave. After this, 10 mL of the co-solvent glycerol (co-solvent) was added. Subsequently, the capping agents were added into the reaction mix - 8 mL of oleylamine (OLA) and 0.080 mL of oleic acid (OA). After sufficient stirring the mixture was placed in a preheated oven for 4 hours. A scheme of the synthesis protocol is shown below (**Sch. 2**).

Scheme 2: Copper nanowire synthesis protocol followed in this work.

After the autoclave had cooled down to room temperature, it was removed from the oven. The reaction mix containing CuNWs was decanted into 50 mL of n-hexane contained in a separating funnel. The nanowires formed, and the waste solution formed an immiscible bilayer in the hexane. To obtain pure nanowires, the hexane layer was slowly washed with 50 mL of hexane three times. The nanowires

were stored in clean hexane. The synthetic process did not require any protective inert atmosphere. CuNWs were synthesised at 120 °C, 140 °C, 160 °C and 180 °C, which were labelled as CuNW-120, CuNW-140, CuNW-160 and CuNW-180.

3.1.1 Synthesis and post treatment chemicals and apparatus

Copper (II) chloride dihydrate ($CuCl_2 \cdot 2H_2O$, ACS reagent), oleylamine (OLA, approximate C-18 content 80 – 90%) and glycerol (≥99%, analytical reagent grade) were purchased from Fisher Scientific. Oleic acid (OA, technical grade 90%), propionic acid (≥99.5%, ACS reagent), n-hexane (≥99%, laboratory reagent grade), formic acid (for synthesis, 98%) and nylon-6 (N-6) pellets were purchased from Merck (Sigma-Aldrich). Ethanol was purchased from Altia Oy and reverse osmosis water was obtained from a Puro^{TM} reverse osmosis water purifier from Avidity Science. The polycarbonate (PC) substrates (0.1 µm pores, 47 mm diameter) were ordered from Pieper Filter GmbH.

Throughout the nanowire synthesis, the following hydrothermal bomb setup from Huanyu was used. The setup was composed of a 100 mL polytetrafluoroethylene-lined container into which all the reagents were added, which was sealed in a stainless-steel autoclave before being placed in the oven for synthesis. The vacuum filtration was conducted using a setup procured from VWR and an N 816 vacuum pump from KNF.

3.2 Characterisation techniques

Specialised characterisation methods are required to analyse copper nanowires due to their nanostructured nature. The surface and overall morphology of the nanowires can be analysed using different types of microscopies. For higher resolution, electron microscopies such as scanning electron microscopy (SEM) and transmission electron microscopy (TEM) are most optimal [45,46], however the length of the nanowires can also be analysed from optical microscopy. To determine the elemental composition, energy dispersive X-ray spectroscopy (EDS) provides a good option for analysis based on SEM images. Methods such as X-ray diffraction (XRD) and X-ray photoelectron spectroscopy (XPS) can be used to analyse the oxidation state and crystalline properties of the nanowires. The use of microscopic and spectroscopic methods in tandem paints a clear picture of the chemistry and structure of the copper nanowires.

3.2.1 SEM and EDS

SEM is a non-destructive tool which is commonly used to find information on the surface morphology and microstructural properties of materials. The operating principle is based on exposing the sample to a high-energy electron beam (1–40 keV) [47], allowing researchers to visualise the sample using high-quality imaging with 1 nm spatial resolution [46]. SEM and electron microscopy, in general, provide high resolution and high magnification imaging of nanomaterials, unlike optical microscopy. The operating principles of an optical and electron microscope are compared in **Fig. 1a.**

To obtain a high-resolution image, SEM imaging must be operated under a vacuum to avoid interactions of electrons with gas molecules, which could derail them from their path [45,46]. The source electron beam emits primary electrons, which are focused into a monochromatic beam and aimed at the sample surface [46]. Magnetic field lenses and metal slits help to confine the primary electrons as they are scanned across the sample surface by scanning coils in a raster pattern [46,48]. When the primary electron beam interacts with the sample surface, a variety of signals are emitted. These include secondary electrons (SEs), backscattered electrons (BSEs), photons (X-rays used for elemental analysis) and visible light [46], which are visualised in **Fig. 1b**. The signals are gathered by detectors, after which the signals are computer manipulated to form a digital image.

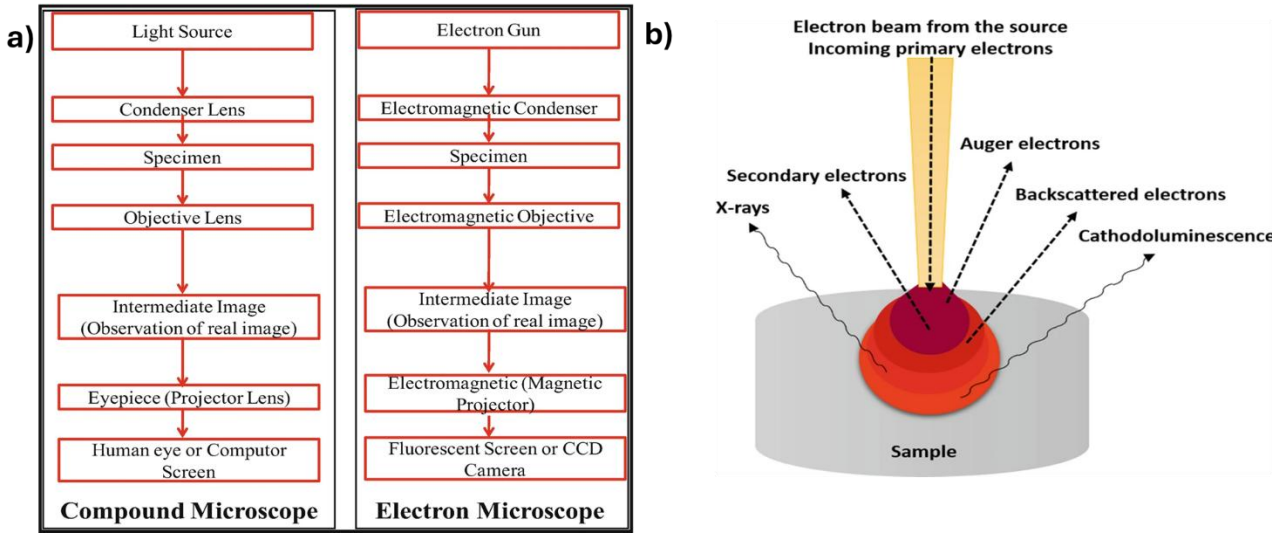

Figure 1: **(a)** Block diagram comparison of optical and electron microscopy. From Y. Javed et al., *TEM for Atomic-Scale Study: Fundamental, Instrumentation, and Applications in Nanotechnology*, Springer Nature, 2018. [45] Reproduced with permission from Springer Nature. **(b)** Interaction of the electron beam with the specimen and the signals emitted from the sample. From K. Akhtar et al., *Scanning Electron Microscopy: Principle and Applications in Nanomaterials Characterization*, Springer Nature, 2018. [46] Reproduced with permission from Springer Nature.

Different information about the sample can be observed based on the signal used to form the image [46]. SEs are considered the most important, as SE images depict sample morphology and topography

most accurately [46]. BSEs are used for imaging multiphase samples, where the contrasts of the image can be used to distinguish between phases [46]. The X-rays that are emitted from the sample each have a specified wavelength, depending on the difference in energy level of the elements [46]. The characteristic X-rays emitted can be detected through energy-dispersive X-ray spectroscopy (EDS), which generates the elemental composition of the sample.

Conductive samples can be imaged directly with minimal preparation, typically yielding high-resolution images. In contrast, non-conductive or poorly conductive samples require additional preparation to ensure good quality imaging. These samples are typically coated with a thin conductive layer, such as gold, carbon, or platinum, using techniques like sputter coating. The conductive coating dissipates accumulated charge, preventing surface charging effects that can affect the image quality to prevent surface charging.

Field emission scanning electron microscopy (FE-SEM) is better for obtaining clear and high-quality images and information about the composition of nanomaterials [46]. It can be used to study comprehensive information about the topography, morphology, orientation of grains, crystallography, arrangement, and composition of nanomaterials. Morphological analysis of the synthesised nanowires was conducted using an FE-SEM (Apreo S, Thermo Fisher Scientific) operating at acceleration voltages of 2 kV and 5 kV. SEM imaging was done mainly using SE detectors. Diameters and lengths of the CuNWs were measured from SEM images. SEM was also used for the imaging of the CuNW-N-6 FCS. EDS was performed to analyse the elemental composition of the CuNW-N-6 FCS.

3.2.2 TEM

Transmission electron microscopy (TEM) is a type of electron microscopy, which is capable of detailed imaging of even smaller samples than SEM. TEM imaging requires a vacuum, similarly to SEM, to prevent electrons from being distracted from their path by contaminants and gases [45]. Multiple different vacuum pumps are used to create the required vacuum in TEM [46]. The operating principle behind TEM is based on focusing a high-energy electron beam through the condenser lens onto the sample — the interaction between the electrons and atoms of the sample forms the desired image at the objective lens [45]. A charge-coupled device (CCD) is placed below the screen to capture and store the image. As the electron beam is focused onto the sample through the condenser lens, extra electrons are filtered out by apertures [45].

High-resolution TEM (HR-TEM) enables higher magnification of samples, making possible the visualisation of minuscule details such as atomic lattices and grain boundaries. Selected Area Electron Diffraction (SAED) can be used to discover crystallographic information from diffraction patterns [45]. The electron gun, which emits and targets an electron beam onto the sample, has two types of emission modes, thermionic emission (TE) and field emission (FE). The FE source of the electron gun is preferred for high-resolution imaging [45].

TEM samples have very specific requirements, especially regarding their size. The sample specimen should be ultra-thin with a typical thickness of ~100 to 200 nm [49], because electrons would not be able to penetrate through a thicker sample [45]. The electron beam could damage hydrated biological samples. Therefore, such samples should be coated in a protective material (usually carbon) [45].

Two different transmission electron microscopes, the JEOL JEM-F200 and JEM-1400 Plus TEM (**Fig. 2a**), were used for high-resolution morphological analysis of the CuNWs. The former was operated at 200 kV voltage and the latter at 80 kV.

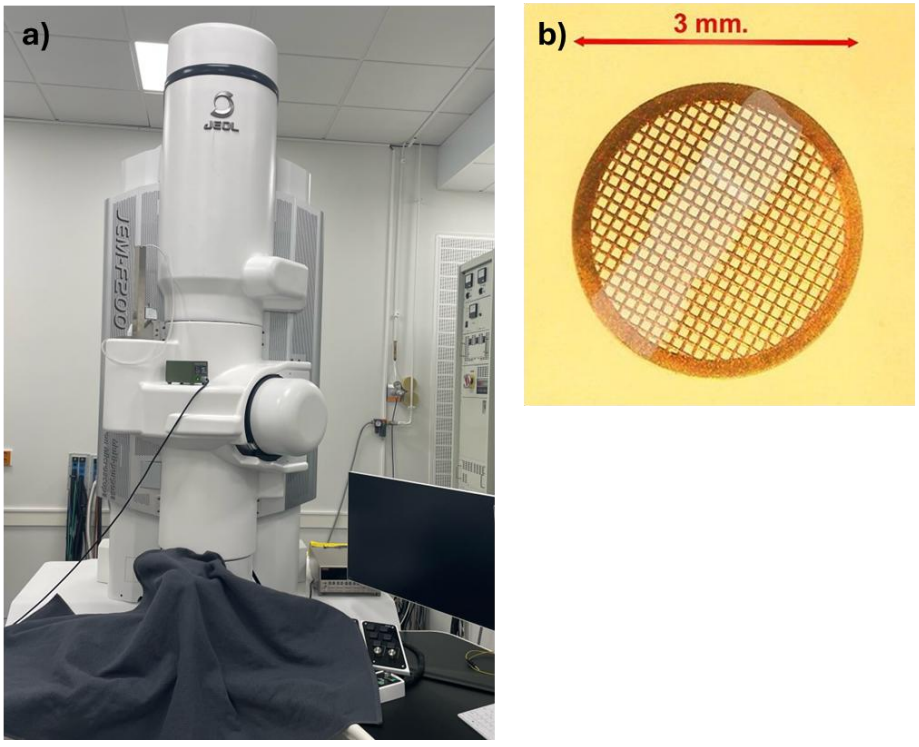

Figure 2: **(a)** JEOL JEM-F200 transmission electron microscope **(b)** TEM grid onto which samples are put.

3.2.3 XRD

X-ray diffraction (XRD) is an analytical technique used for determining the elemental composition, crystallinity and crystal phases of materials. The technique operates on the principle that monochromatic X-ray beams interact with the regularly arranged atoms in the crystal lattice of a material [50]. During this interaction, interference occurs at specific angles that satisfy Bragg's law [50], shown in **Eq. 1** [51].

$$Bragg's\ Law, \qquad n\lambda = 2d\sin\theta \tag{1}$$

Where, λ = X-ray source wavelength = 0.15406 nm; θ = angle of diffraction; d = inter-planar spacing

By recording the angles and intensities of the diffracted beams, a characteristic diffraction pattern is generated for the material. The pattern, presented as intensity versus 2θ, can be used to obtain interplanar spacings (d-values) and lattice parameters [50]. It can also be used to identify crystalline phases by comparing experimental peaks with standard reference patterns available in databases like the International Centre for Diffraction Data (ICDD) database.

In this work, XRD measurements were conducted using a Panalytical Empyrean X-ray diffractometer using a PIXcel3D solid state area detector. Data was collected over a 2θ range of 30-80° at a scan rate of 2° min^{-1}. A schematic of the basic operation principle (**Fig. 3a-b**) and an image of the instrument used in this work (**Fig. 3c**) can be found below. A typical XRD system consists of three main components: an X-ray source, a sample stage, and a detector. The X-ray source emits an X-ray beam with a single wavelength towards the sample. Upon interaction with the crystal lattice, the diffracted X-rays are captured by the detector, which records both their intensity and angle of diffraction. Variations in atomic arrangement and chemical composition lead to unique diffraction patterns for different phases, enabling detailed structural characterisation [50].

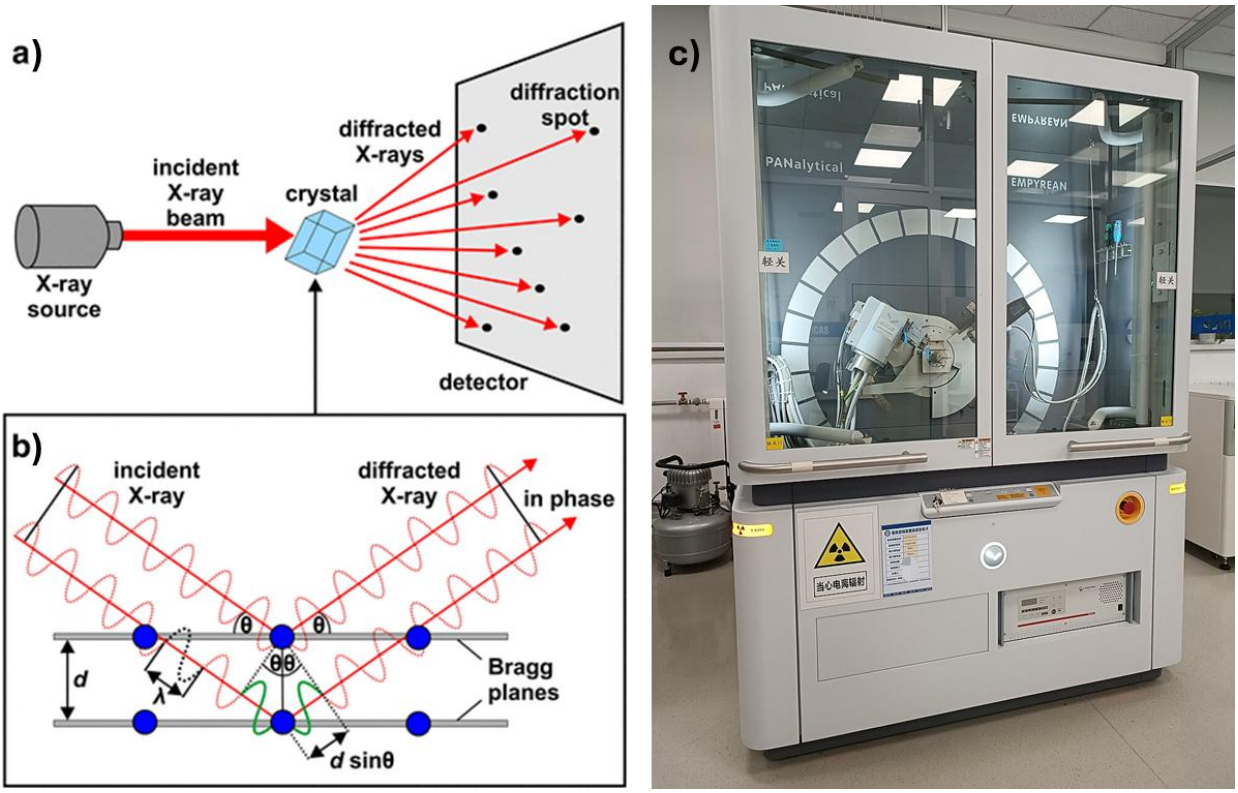

Figure 3: Schemes of XRD operation principle reproduced from Bijelic et al.'s work [52] using CC BY 4.0 licence **(a)** Basic scheme of an X-ray diffraction experiment. **(b)** Diffraction according to Bragg's Law. **(c)** Empyrean Pananalytical XRD, like the one used in our work. Reproduced from Sufangxi, CC BY-SA 4.0 via Wikimedia Commons.

3.2.4 XPS

X-ray photoelectron spectroscopy (XPS) is an analytical technique that provides quantitative information on material properties from the top few nanometres of a material's surface. XPS is a type of emission spectroscopy, namely spectroscopy based on emitted radiation or particles from a material [53]. The type of emission utilised in XPS is X-rays. When X-rays of a specific energy hit a sample's surface, the electrons can be ejected from any of the electronic states, and their kinetic energy is described in **Eq. 2** [53]. The binding energy can be calculated using the kinetic energy of emitted electrons, from which different material properties such as elemental composition and bonding types can be identified [53]. Mg Kα and Al Kα are most used sources of X-rays in commercial XPS systems [53].

$$E_{B.E.} = h\nu - K.E. - \phi \qquad \mathbf{2}$$

XPS was carried out using a Thermo Scientific Nexsa instrument equipped with a monochromatised Al Kα X-ray source and a dual-beam charge compensation system [54]. The survey spectra were scanned using 200 eV pass energy, and the high-resolution spectra were scanned using 50 eV pass energies. All the spectra acquired were deconvoluted using the CasaXPS curve-fitting software using Shirley background and were corrected for charge shift with reference to the adventitious carbon positioned at 284.8 eV. Images of the instrument used in this work (**Fig. 4a**) and the sample holder used to load the samples into the instrument (**Fig. 4b**) can be found below.

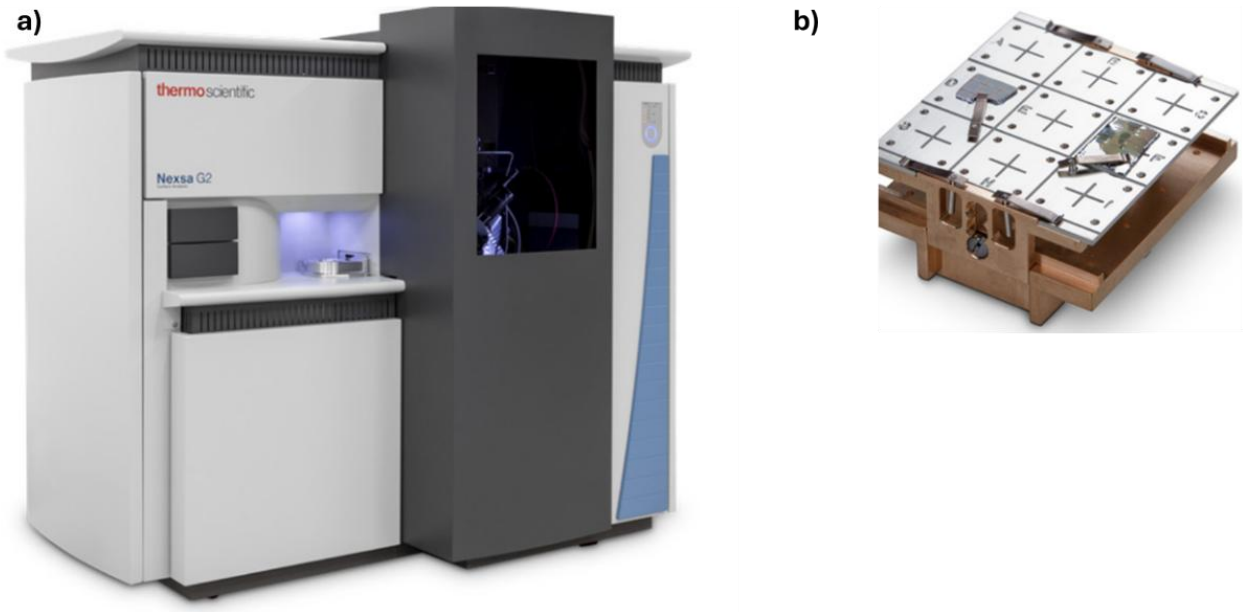

Figure 4: Images reproduced from the Nexsa G2 Surface Analysis System datasheet [54]. **(a)** Thermo Scientific Nexsa XPS instrument **(b)** sample holder for XPS samples.

3.3 Film durability and sensor testing apparatus

A TA.XT.plus100C texture analyser was used for the capacitive curvature sensing and cyclic durability tests of the CuNW-N-6 sensors and the mechanical durability tests of CuNW-PC films. For the mechanical durability tests the height of the texture analyser was calibrated to 1.5 cm, resulting in an active surface area of 1.5 cm × 1.2 cm experiencing compression during the measurements. For the curvature sensor durability tests, the height of the texture analyser was calibrated to 2 cm, resulting in an active surface area of 2 cm × 1.5 cm experiencing compression during the measurements. The relative change in resistance and capacitance was measured using the LCR meter (GW-INSTEK LCR-6300). A testing signal of 1 V at 1 kHz was employed for all measurements on the LCR meter. The texture analyser and LCR meter setup is shown in **Fig. 5** below.

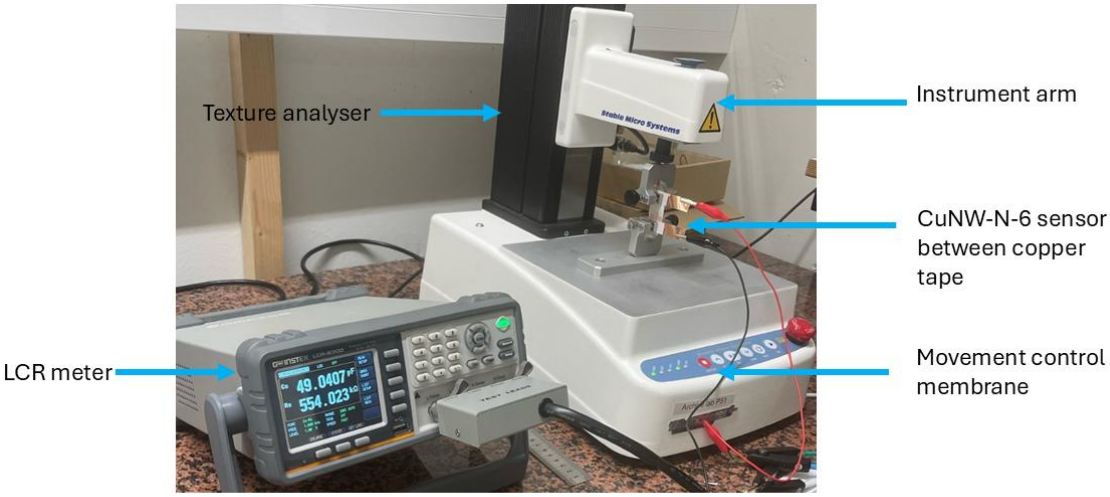

Figure 5: Picture of LCR meter (left) and texture analyser (right) setup.

The sheet resistance of the CuNW-PC films was measured using an Ossila four-point probe system (**Fig. 6**), which had a probe spacing of 1.27 mm. A 4-point probe conductivity measurement device can be used to study the electrical properties of thin materials. It uses a line of four small probes, which are lowered onto the surface of the sample, to measure sheet resistance. The two outermost probes inject a current from a current source, while the innermost probes measure the voltage.

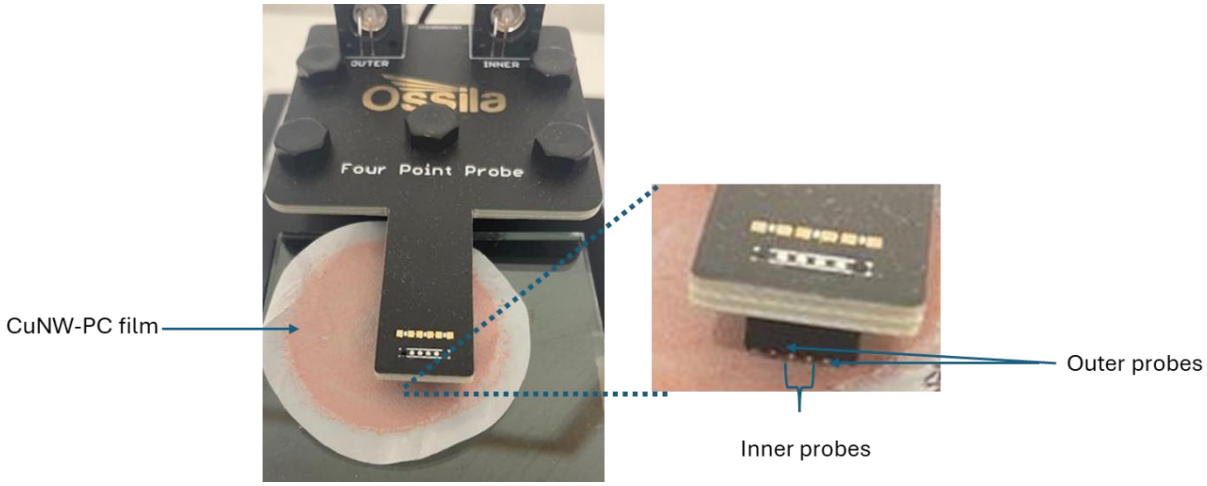

Figure 6: Ossila four-point probe system, adapted from [30].

Thermal durability testing was conducted on a hot plate, and conductivity at 20 °C temperature intervals was measured using an 87V true RMS multimeter obtained from Fluke.

3.4 Fabrication of Conductive Copper Nanowire-Polycarbonate Surfaces

3.4.1 Fabrication of films for durability testing

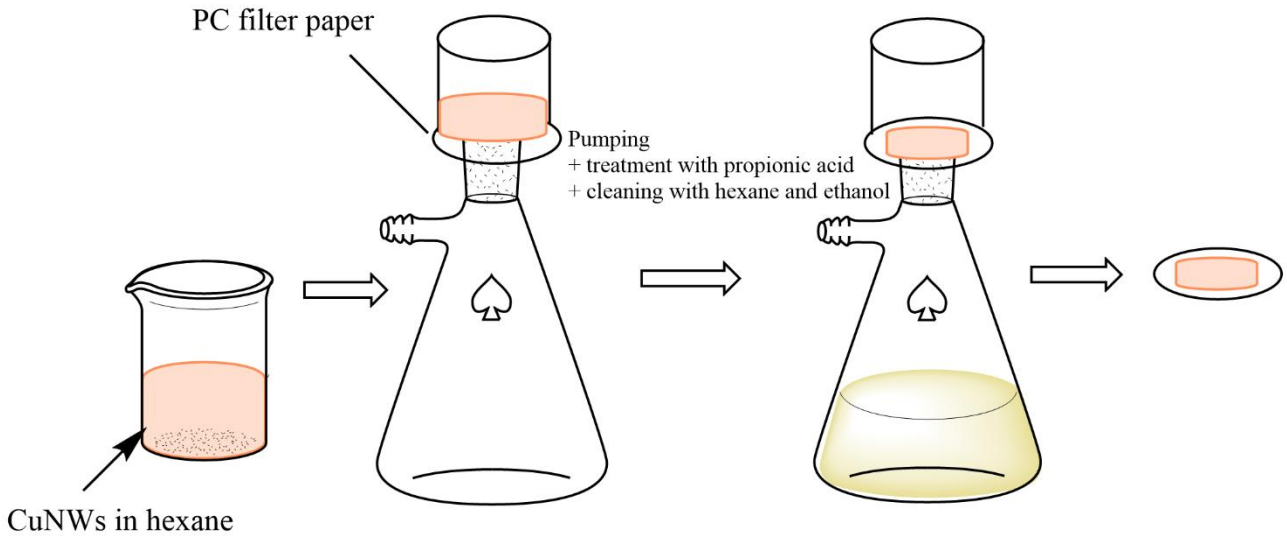

Scheme 3: Fabrication of CuNW-PC film using vacuum filtration.

To fabricate nanowire-based substrates, a copper nanowire dispersion was prepared in 50 mL hexane at a concentration of ~3 mg mL^{-1}. The nanowire suspension (3 mL) was transferred into a vacuum filtration setup and filtered through a polycarbonate (PC) substrate. This formed a uniform nanowire film on the N-6 surface that covered a surface area of 9.62 cm^2. To remove the oxide layer and residual organics, the film was treated with a solution (3 mL) of propionic acid: ethanol (1:29) for 15 seconds. Finally, the solution was filtered out and gently washed three times with hexane (3 × 1 mL), after which it was dried for further analysis. The full fabrication procedure of the CuNW-PC films is depicted in **Sch. 3** above. Hereafter, CuNW-PC will stand for copper nanowires on polycarbonate surfaces.

3.4.2 Fabrication of CuNW-nylon 6 FCS

Vacuum filtration was also used to fabricate a copper nanowire (CuNW) based FCS, using an electrospun nylon-6 (N-6) nanofibre surface the substrate for CuNW deposition. A 5 mL CuNW suspension in hexane (~3 mg mL^{-1}) was filtered through a circular N-6 substrate. resulting in the formation of a uniform nanowire film on the N-6 surface, covering an area of 9.62 cm^2. The film was treated with 3 mL of a propionic acid: hexane solution (1:29) for 15 seconds. This was followed by cleaning twice with 3 mL of ethanol, followed by filtration and drying under vacuum. Hereafter, CuNW-N-6 will stand for copper nanowires on N-6 surfaces.

3.4.3 Fabrication of curvature sensor

For the fabrication of a copper nanowire-based curvature sensor, two identical pieces of CuNW-N-6 FCS were used as electrodes with dimensions of approximately 1.5 cm × 3 cm. One N-6 nanofibre surface was used as the dielectric layer with the dimensions 2 cm × 2 cm. The dielectric layer was sandwiched between the two CuNW-N-6 surfaces, with their conductive sides facing inward. Then, the sensing region was encapsulated with cellulose tape to preserve it for further use. The active sensing region was maintained at 1.5 cm × 2 cm. A scheme of the fabrication of the sensor is shown below (**Sch. 4**).

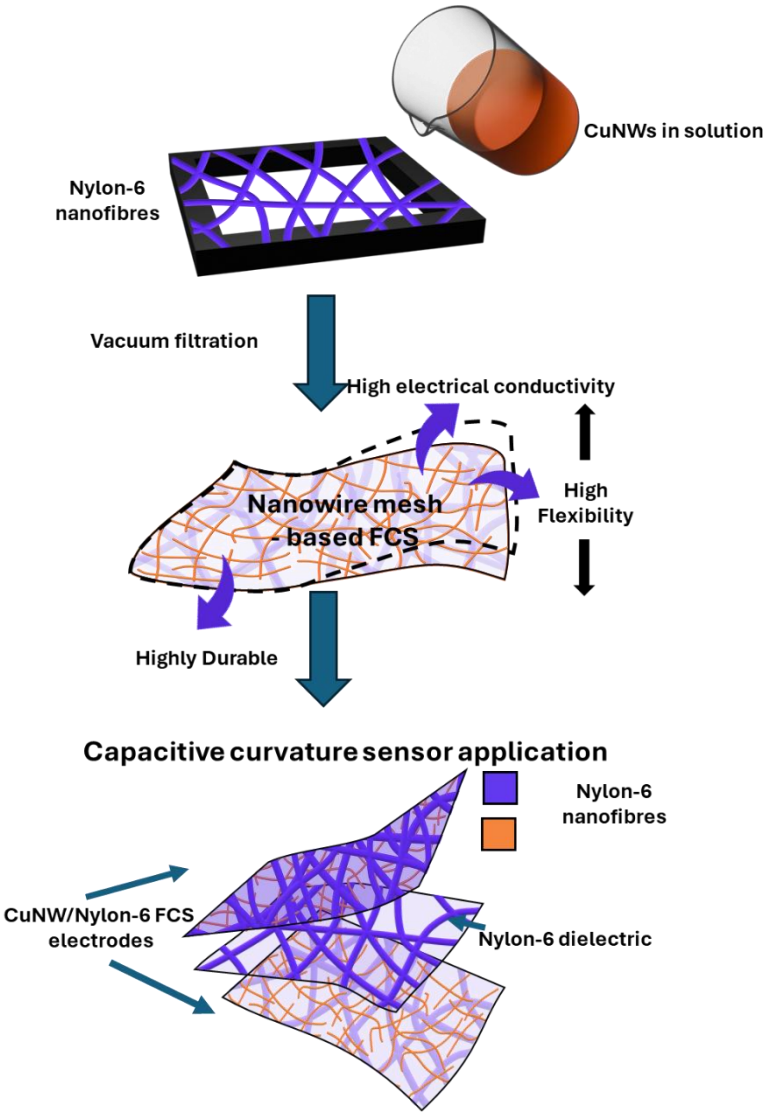

Scheme 4: Fabrication of CuNW-Nylon-6 FCS step by step.

4 Results and discussion

The thesis work is focused on synthesising copper nanowires at temperatures of 120 °C, 140 °C, 160 °C and 180 °C, aiming to study the effect of this variation on nanowire properties and performance in flexible electronic devices, as in the article it is based on [30]. This chapter will commence with the discussion of the characterisation of the synthesised CuNWs, followed by the various durability studies of CuNW-polycarbonate films and CuNW-nylon-6 based curvature sensors for each synthesis temperature.

We synthesised ultra-long copper nanowires using a solution-based polyol method [30]. In this approach, polyols serve as both solvents and reducing agents, preventing oxidation during synthesis, making the method ideal for industrial and research applications. We used glycerol as the polyol; however, its reduction potential alone was insufficient. Therefore, glucose was introduced as an additional reducing agent to facilitate the reduction of copper (II) salts to metallic copper nanowires (Cu^0). To control the nanowire structure and morphology, oleylamine and oleic acid were used as capping and co-capping agents, respectively. Their presence guided the asymmetrical growth of ultra-long nanowires. To enhance durability, the reaction was performed at various temperatures to improve the intrinsic quality of the nanowires.

4.1 Morphology and chemical composition

To characterise the morphology of the copper nanowires, scanning electron microscopy (SEM) and transmission electron microscopy (TEM) were employed. X-ray diffraction (XRD) and X-ray photoelectron spectroscopy (XPS) were used to characterise the chemical composition and oxidation states of the CuNWs.

4.1.1 Morphology of CuNWs

The morphology of the synthesised nanowires was investigated using electron microscopy, as shown in **Figures 7, 8, 9** and **10,** showing SEM images of CuNW-120, 140, 160 and 180, respectively. Analysis of the scanning electron micrographs confirms the formation of ultra-long nanowires, with only a few undesired byproducts. These byproducts likely resulted from non-instantaneous nucleation and diffusion-limited growth; phenomena commonly observed in most synthetic methods [2]. The average diameter of the nanowires was determined by analysing ~100 nanowires from SEM images, while 8-10 nanowires were analysed to obtain the length distribution.

Fig. 7 shows SEM images taken of CuNW-120 at various magnifications, giving insight into its morphology. The low-magnification image (**Fig. 7a)** shows an overall view of the randomly distributed CuNW network. A representative CuNW-120 nanowire used for average length measurements is shown in **Fig. 7b** - the average length of the nanowires was 24 ± 13 µm.

Figs. 7c and **7d** are higher magnification images of **Fig. 7a**, offering a more detailed view of individual nanowire morphology. From **Fig. 7c**, the diameter distribution of the nanowires is fairly uniform. By measuring diameters of ~100 CuNW-120 nanowires, this observation was confirmed, as the average diameter was measured as 43 ± 6 nm, displaying relatively uniform diameter distribution. The corresponding Gaussian plot of the diameter distribution, shown in the inset of **Fig. 7c**, further confirms the uniformity in diameter. The average length was measured as 24 ± 13 µm, which is the shortest average length of the nanowires prepared at different reaction temperatures. **Fig. 7d** shows that the NWs have fairly rough surfaces, despite the uniformity in diameter distribution.

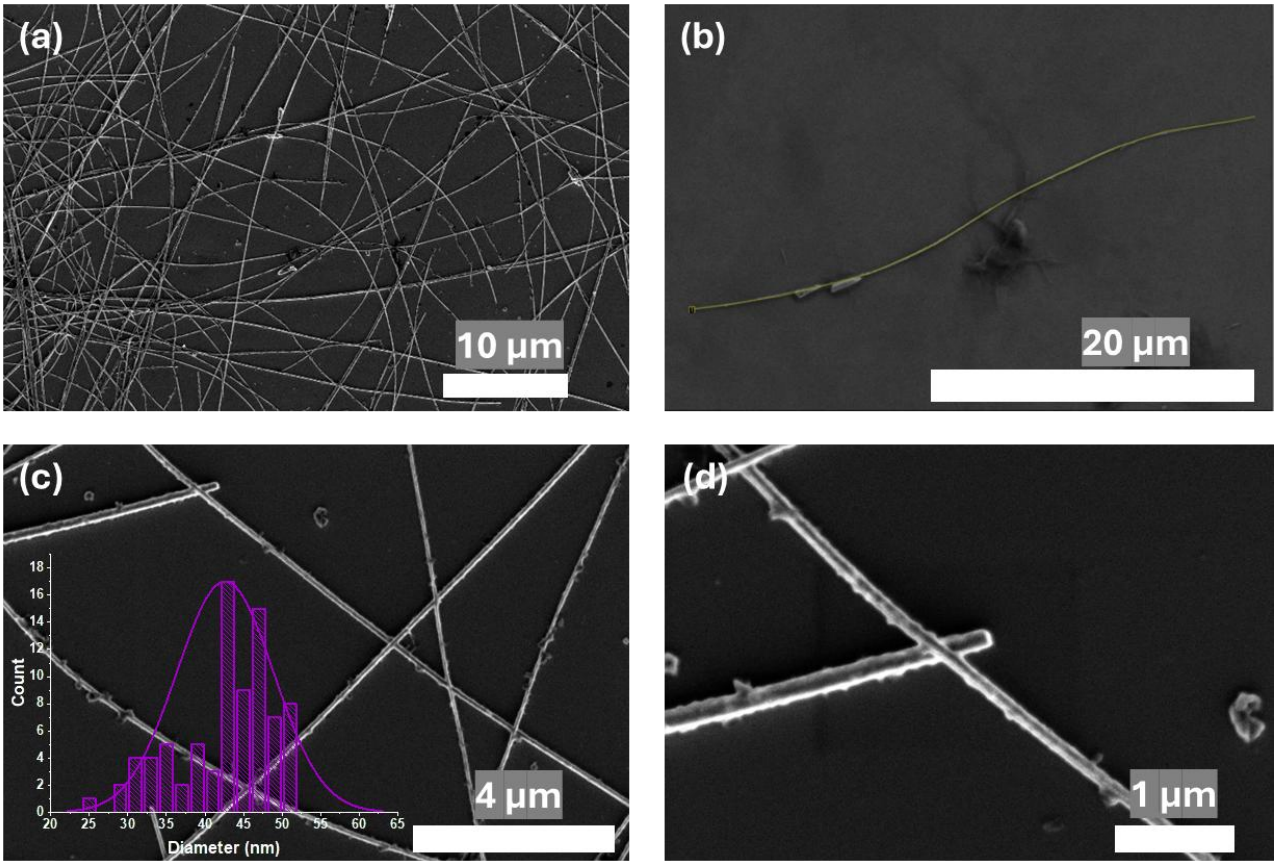

Figure 7: CuNW-120 morphology depicted using SEM micrographs **(a)** Overview of CuNW-120 nanowires **(b)** An SEM micrograph used for CuNW-120 length measurement **(c)** Zoomed in SEM micrograph of CuNW-120 nanowires with an inset of the Gaussian diameter distribution plot **(d)** SEM micrograph showing the surface morphology of CuNW-120 nanowires.

Fig. 8 shows SEM images taken of CuNW-140. **Fig. 8a** shows an overall view of multiple CuNWs, while **Figs. 8c** and **8d** are higher magnification SEM images better portraying the morphology of single CuNW-140 nanowires. In **Fig. 8c**, the diameter distribution is still fairly uniform, which was confirmed after diameters of ~100 CuNW-140 nanowires were measured and the average diameter value of 61 ± 18 nm was obtained. A Gaussian plot of the diameter distribution is shown in the inset of **Fig. 8c**. Interestingly, both the diameter thickness and the average length of the nanowires grew, with length increasing significantly to 83 ± 31 µm. One of the nanowires measured for the average length calculation shown in **Fig. 8b**. **Fig. 8d** shows that the NWs have clearly smoother surfaces than those synthesised at 120 °C.

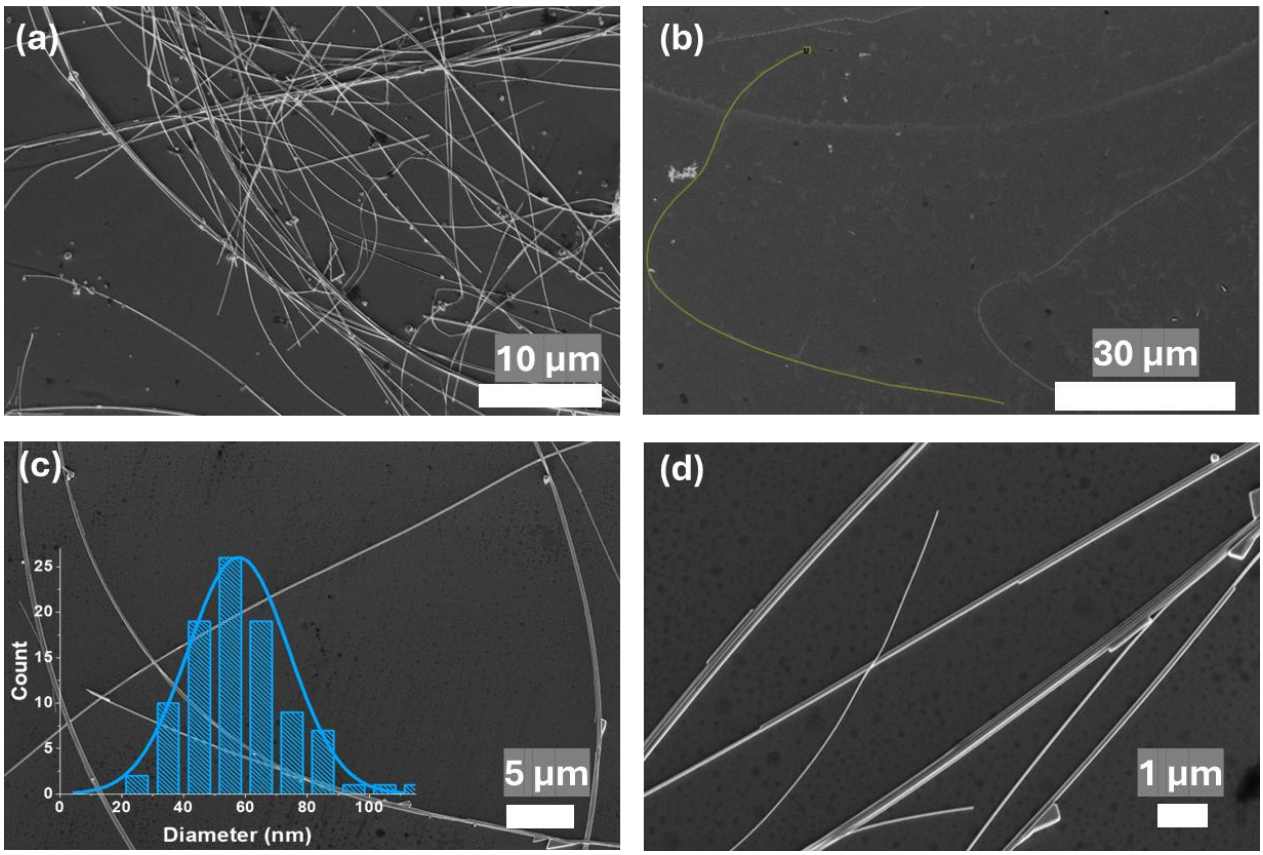

Figure 8: CuNW-140 morphology depicted using SEM micrographs **(a)** Overview of CuNW-140 nanowires **(b)** An SEM micrograph used for CuNW-140 length measurement **(c)** Zoomed in SEM micrograph of CuNW-140 nanowires with an inset of the Gaussian diameter distribution plot **(d)** SEM micrograph showing the surface morphology of CuNW-140 nanowires.

Fig. 9 shows SEM images taken of CuNW-160. **Fig. 9a** shows an overall view of multiple CuNWs, while **Figs. 9c** and **9d** are higher magnification SEM images of **Fig. 9a**, better portraying the morphology of single CuNW-160 nanowires. After diameters of ~100 CuNW-160 nanowires were measured and the average diameter value of 66 ± 27 nm was obtained, indicating a further increase in diameter thickness with higher reaction temperature. A Gaussian plot of the diameter distribution

is shown in the inset of **Fig. 9c**. As with CuNW-140, both the diameter thickness and the average length of the nanowires grew, with the length increasing significantly to 128 ± 32 µm. One of the nanowires measured for the average length calculation shown in **Fig. 9b**. **Fig. 9d**, proves that the NWs have smoother surfaces than those synthesised at 120 °C and 140 °C.

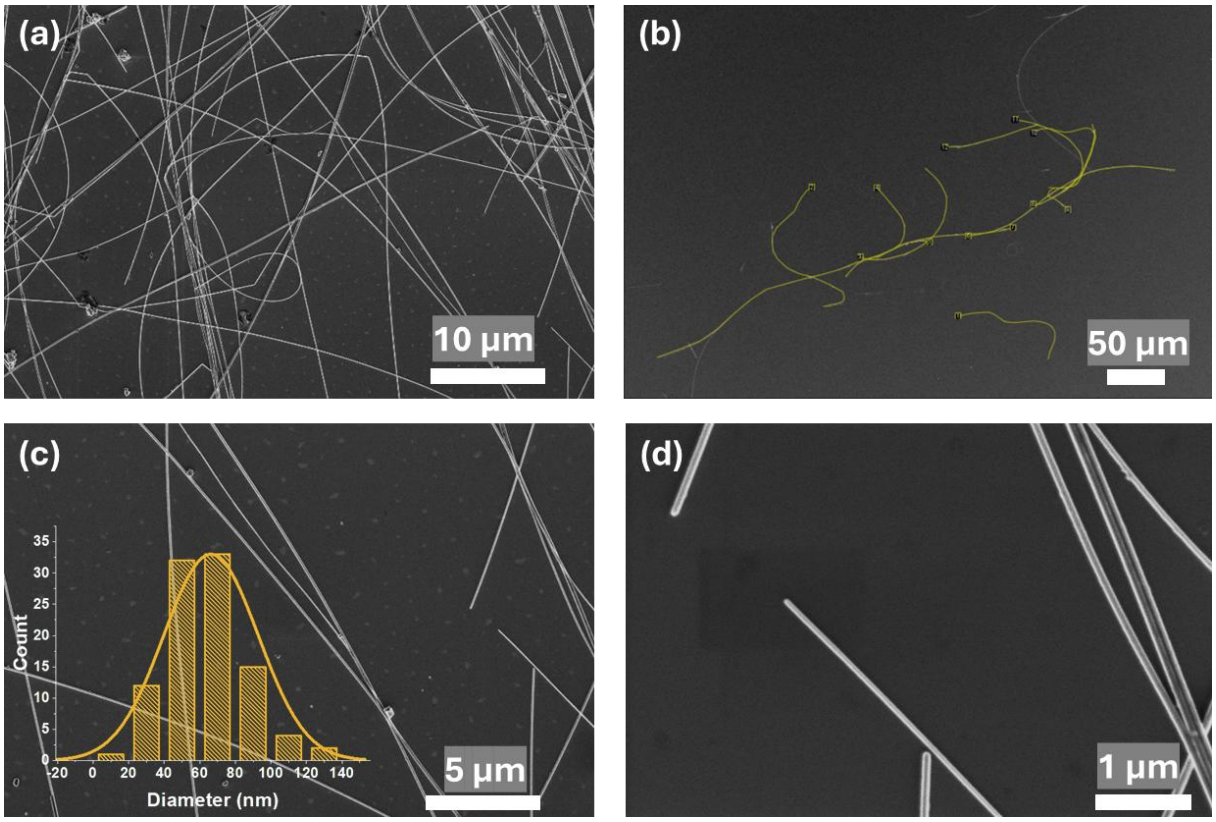

Figure 9: CuNW-160 morphology depicted using SEM micrographs **(a)** Overview of CuNW-160 nanowires **(b)** An SEM micrograph used for CuNW-160 length measurement **(c)** Zoomed in SEM micrograph of CuNW-160 nanowires with an inset of the Gaussian diameter distribution plot **(d)** SEM micrograph showing the surface morphology of CuNW-160 nanowires.

Fig. 10 shows SEM images taken of CuNW-180. **Fig. 10a** shows an overall view of multiple CuNWs, while **Figs. 10c** and **10d** are higher magnification SEM images of **Fig. 10a**, better portraying the morphology of single CuNW-180 nanowires. After diameters of ~100 CuNW-180 nanowires were measured and the average diameter value of 74 ± 31 nm was obtained, indicating further increase in diameter thickness with higher reaction temperature. A Gaussian plot of the diameter distribution is shown in the inset of **Fig. 10c**. Interestingly, the average nanowire length did not grow any more, and the average value obtained was 64 ± 18 µm. Many of the nanowires measured for the average length calculation are shown in **Fig. 10b**. **Fig. 10d** shows that the NWs have very smooth surfaces, like those synthesised at 160 °C.

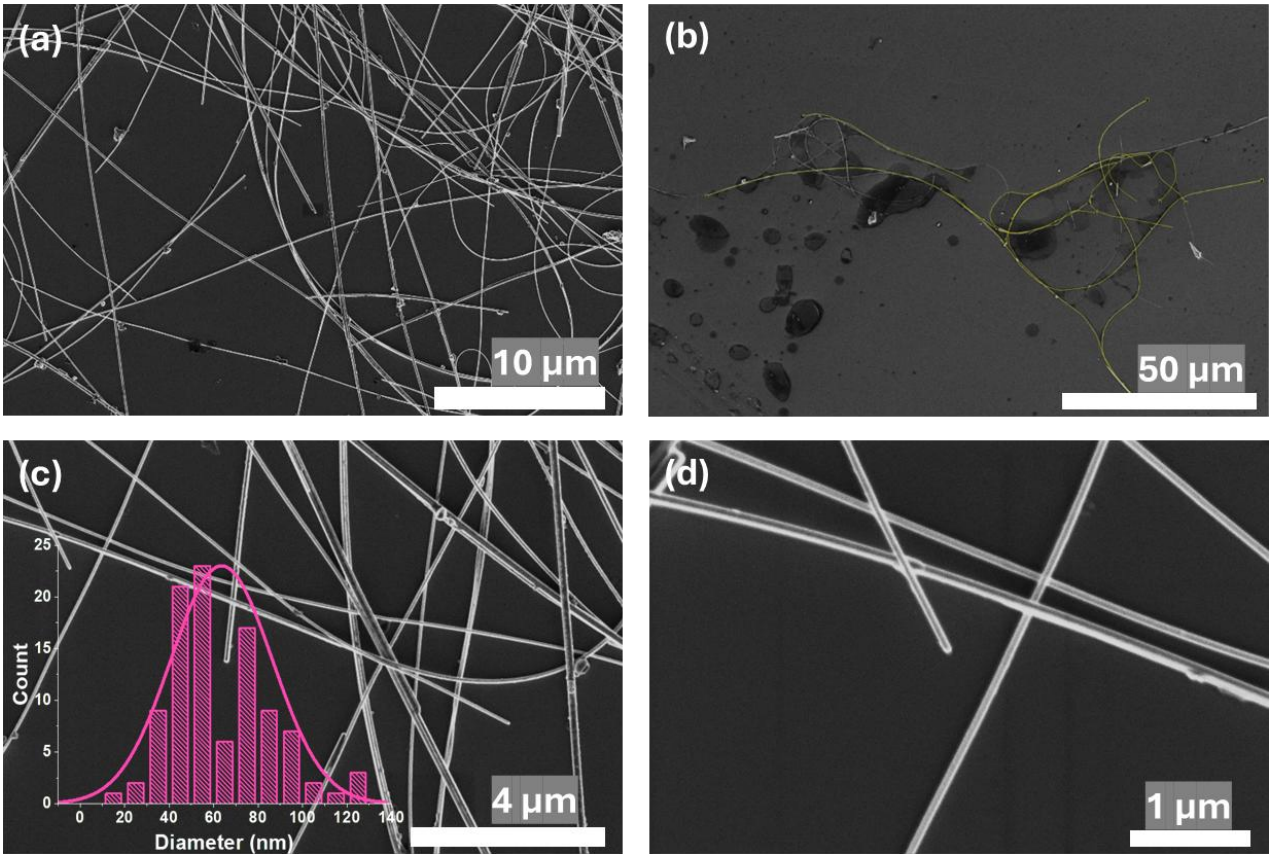

Figure 10: CuNW-180 morphology depicted using SEM micrographs **(a)** Overview of CuNW-180 nanowires **(b)** An SEM micrograph used for CuNW-180 length measurement **(c)** Zoomed in SEM micrograph of CuNW-180 nanowires with an inset of the Gaussian diameter distribution plot **(d)** SEM micrograph showing the surface morphology of CuNW-180 nanowires.

In conclusion, the nanowires prepared at 120 °C showed the thinnest and most uniform diameters. However, the diameters increased and uniformity decreased when the nanowires were synthesised at higher temperatures. In fact, the CuNW-180 nanowires show a range from very narrow nanowires to very thick nanowires with additional nanoparticles in the mix. The average length increased with reaction temperature, with the average length for CuNW-120 being 24 ± 13 µm, which increased to 128 ± 32 µm for CuNW-160. Interestingly, when the reaction temperature exceeded 160 °C, the average length of the nanowires decreased, with the length measuring 64 ± 18 µm for CuNW-180. Consequently, the length-to-diameter aspect ratios of the nanowires were calculated as 558, 1356, 1939, and 865, for CuNW-120, CuNW-140, CuNW-160 and CuNW-180, respectively. The length and diameter distributions are plotted together in **Fig. 11**, evidencing that the change in morphology is correlated with temperature.

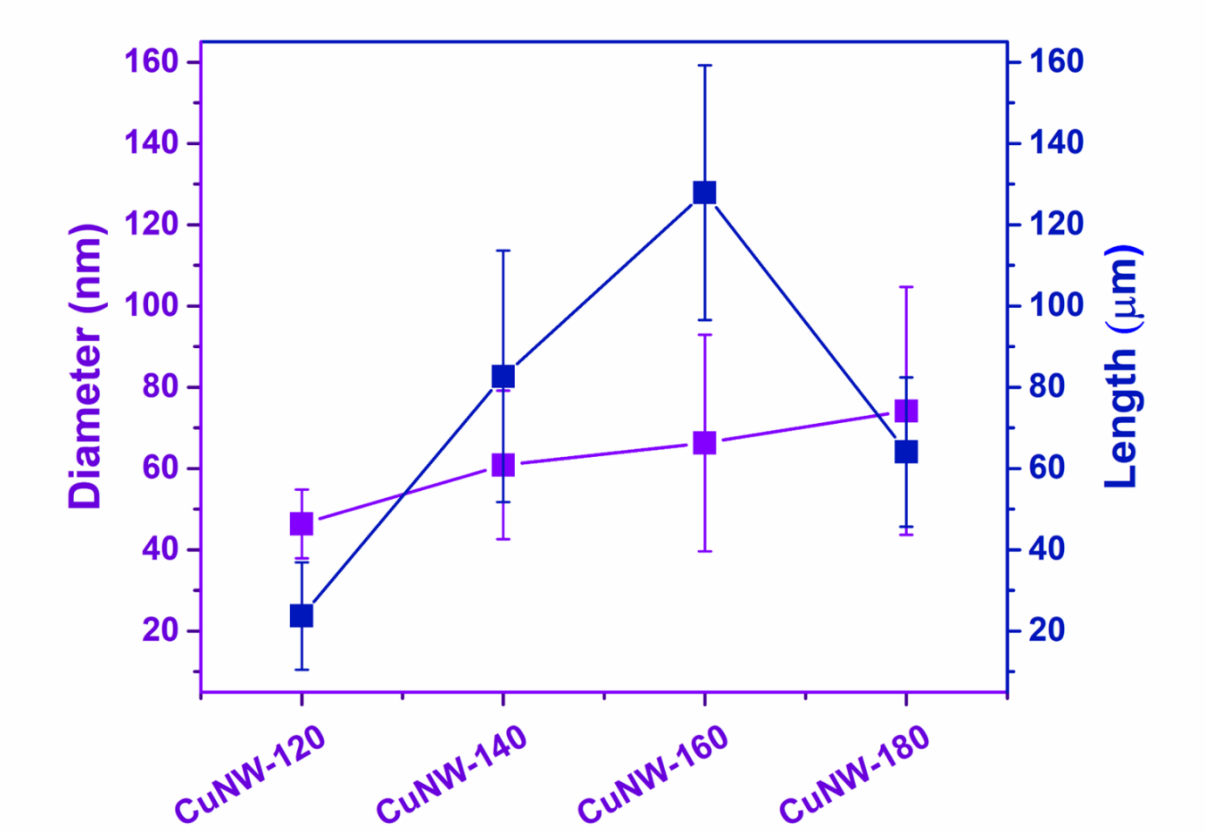

Figure 11: Length and diameter distribution plots of all copper nanowires.

In **Fig. 12 (a-c)** the TEM analysis of CuNW-120 nanowires is displayed. It shows a significantly smaller diameter than the nanowires synthesised at other temperatures, which matches with the trend observed from the SEM images. The rough surface depicted in **Fig. 12a** is in line with the surface oxidation expected from CuNW-120 as well as with the surface roughness observed in **Fig. 7d**. **Fig. 12b** shows the high-resolution TEM (HR-TEM) analysis of the core of a CuNW-120 nanowire. The lattice spacings were measured to be ~0.21 nm and ~0.24 nm, respectively, meaning that they are (111) crystalline planes of both metallic copper (Cu^0) and copper oxide. The selected area diffraction (SAED) pattern shown in **Fig. 12c** displays the crystalline planes characteristic to crystalline copper - (220), (200) and (111).

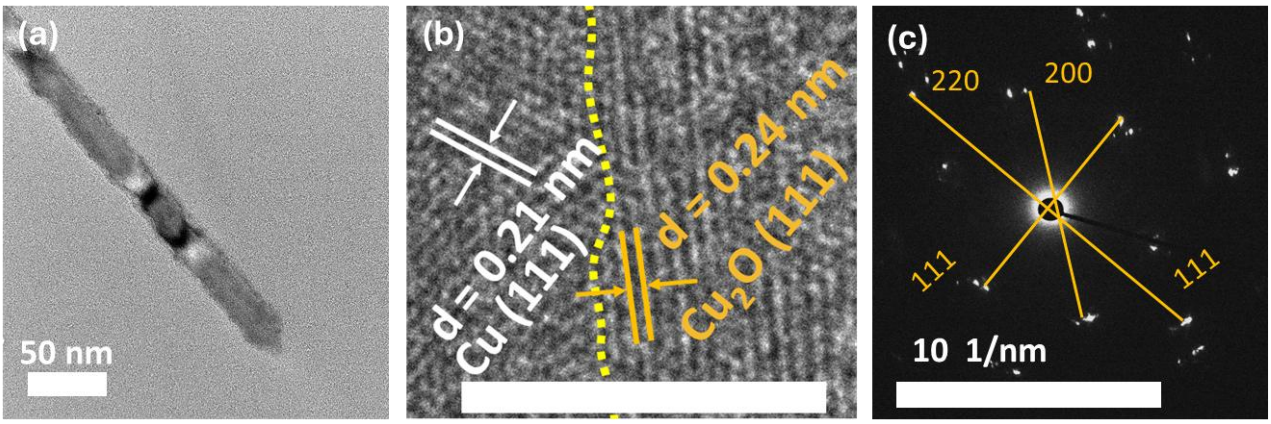

Figure 12: CuNW-120 TEM analysing on **(a)** surface smoothness, **(b)** lattice spacing (scale bar 5 nm) **(c)** SAED pattern. Adapted from [30].

The TEM analysis of CuNW-140 nanowires is displayed in **Fig. 13 (a-c)**. **Fig. 13a** shows a significantly thicker diameter than the nanowires synthesised at 120 °C, aligning with the trend observed from the SEM images. The nanowire surface depicted in **Fig. 13a** is a bit smoother than that of the CuNW-120 nanowire but still exhibits clear signs of surface roughness. **Fig. 13b** shows the HR-TEM analysis of the core of a CuNW-140 nanowire. A lattice spacing was measured to be ~0.21 nm, corresponding to the (111) crystalline plane of Cu^0. However, a lattice spacing of ~0.24 nm, corresponding to copper oxide, was also measured. The SAED pattern in **Fig. 13c** shows the crystalline planes (220) and (111), which are characteristic to crystalline copper.

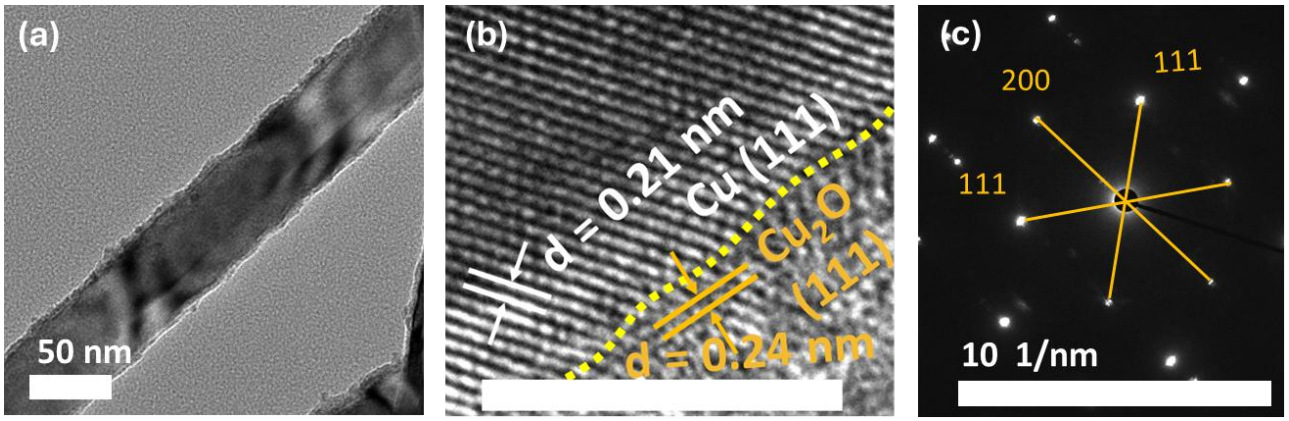

Figure 13: CuNW-140 **(a)** surface smoothness, **(b)** lattice spacing (scale bar 5 nm) **(c)** SAED pattern. Adapted from [30].

The TEM analysis of CuNW-160 nanowires is displayed in **Fig. 14 (a-c)**. **Fig. 14a** shows a thicker diameter than the nanowires synthesised at lower temperatures, aligning with the trend observed from the SEM images. The nanowire surface depicted in **Fig. 14a** is significantly smoother than that of the CuNW-140 and 120 nanowires, which also matches the surface smoothness trend in the SEM images.

Fig. 14b shows the HR-TEM analysis of the core of a CuNW-160 nanowire. The lattice spacing was measured to be ~0.21 nm, corresponding to the (111) crystalline plane of Cu^0. The SAED pattern in **Fig. 14c** shows corresponding information, with crystalline planes (200) and (111) identified.

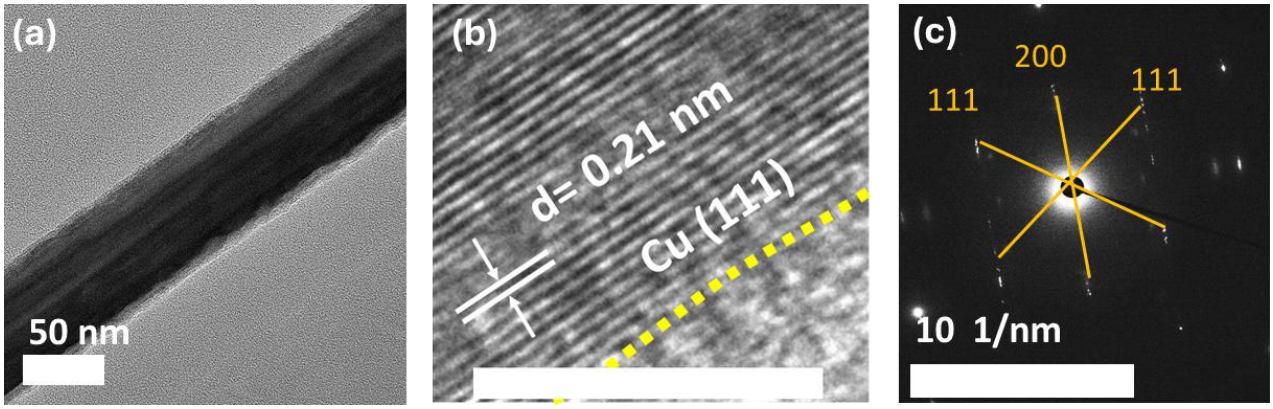

Figure 14: CuNW-160 **(a)** surface smoothness, **(b)** lattice spacing (scale bar 5 nm) **(c)** SAED pattern. Adapted from [30].

In **Fig. 15 (a-c)** the TEM analysis of CuNW-180 nanowires is displayed. **Fig. 15a** shows a thicker diameter than the nanowires synthesised at lower temperatures, aligning with the trend observed from the SEM images. The nanowire surface depicted in **Fig. 15a** is clearly the smoothest of all the nanowires, matching the surface smoothness trend in the SEM images. **Fig. 15b** shows the HR-TEM analysis of the core of a CuNW-180 nanowire. The lattice spacing was measured to be ~0.21 nm, corresponding to the (111) crystalline plane of Cu^0. The SAED pattern shown in **Fig. 15c** shows corresponding information, with crystalline planes (220), (200) and (111) identified.

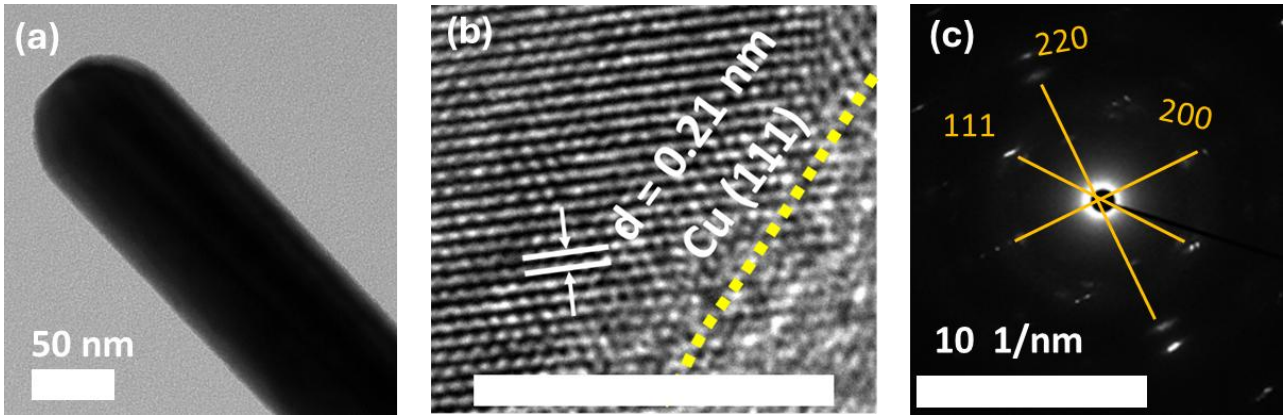

Figure 15: CuNW-180 **(a)** surface smoothness, **(b)** lattice spacing (scale bar 5 nm) **(c)** SAED pattern. Adapted from [30].

From the TEM and SEM images of the nanowires, it can be observed that the surface smoothness of the nanowires improved with increasing reaction temperature. CuNW-120 showed poor surface smoothness (**Fig. 12a** and **Fig. 7d**), CuNW-140 showed adequate surface smoothness with clear

roughness in the TEM image (**Fig. 13a** and **Fig. 8d**), CuNW-160 showed high surface smoothness (**Fig. 14a** and **Fig. 9d**) and CuNW-180 showed the highest surface smoothness (**Fig. 15a** and **Fig. 10d**). Hemmati et al. showed that higher temperatures accelerate Ag^0 nucleation via rapid conversion of ethylene glycol to glycolaldehyde [55]. Based on this, the lower reaction temperatures (120 – 140 °C) could lead to insufficient reduction of Cu^{2+} from the precursor copper salt to form metallic Cu^0 nanowires. This could have resulted in the formation of nanowires with rougher surfaces at lower reaction temperatures. To analyse the crystal lattices, high-resolution TEM analysis was also performed, as shown in **Figures 7b, 8b, 9b** and **10b**. All nanowires exhibited lattice planes corresponding to crystalline copper nanowires. The measured lattice plane spacings were 0.21 nm, corresponding to (111) planes of crystalline metallic copper. CuNW-120 and CuNW-140 also exhibited lattice spacings of 0.24 nm, corresponding to the (111) planes of copper oxide, which could also be due to the insufficient reduction of the copper salt precursor.

The increasing diameter and increasing length (until 160 °C) trend could be due to the faster growth along the diameter and length as it increases with temperature. Additionally, at higher temperatures, nanowire growth proceeds along both the length and side facets, resulting in longer and wider nanowires. However, a large deviation from the average diameters and reduced nanowire length was also observed with increase in temperature. This could be due to the decomposition of the capping agents OLA and OA [56]. The OLA/OA pair binds to the metal facets based on the surface-energy order, which is (111) < (100) < (110) [57]. Therefore, side facets i.e. (100), which are responsible for controlling diameter, are preferentially passivated for further growth. This produces narrower diameters, elongated nanowires, and a larger crystal size at elevated temperatures. They work best at lower temperatures, while they start decomposing slowly at lower temperatures, and beyond 160 °C their degradation is more significant [56]. Therefore, elongation along the length of the nanowires was suppressed, while growth along the diameter was preferred at 180 °C. This was also evidenced from the increasing crystallite sizes derived from XRD, leading to the formation of smoother ultra-long nanowires till 160 °C [58].

4.1.2 Chemical composition of CuNWs

To confirm the trends in crystallinity and purity of synthesised nanowires analysed from TEM and SEM images, XRD patterns were obtained (**Figure 16**). All the nanowires exhibited three major crystalline peaks at 2θ values of 43.3°, 50.5°, and 73.5°. These peaks correspond to the (111), (200), and (220) diffraction planes of copper [57] and confirm that all the nanowires are crystalline as seen

in the SAED patterns. CuNW-120 shows a weak diffraction peak at 2θ ~ 36.3°. This can be attributed to the presence of Cu_2O (111) (JCPDS 05-0667) in minor quantities [59].

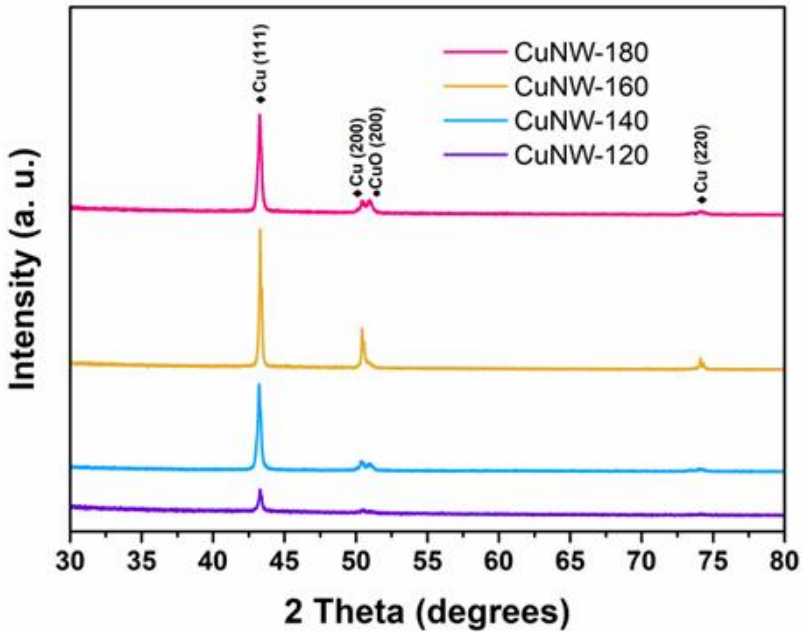

Figure 16: XRD patterns of all copper nanowires directly after synthesis.

A crystallite is a region of solid matter that has a uniform crystal structure and consistent crystallographic orientation [60]. Crystallites form during material synthesis, such as during solidification or chemical reactions [60]. They are bonded together by irregular interfaces known as grain boundaries, forming a crystalline solid [60]. This makes crystallite size a structural parameter, with quantitative importance. Crystallites can range in size from several nanometres to several millimetres, with crystallites with diameters ranging from 1- 100 nm classified as nanocrystalline [60].

In this study, the average crystallite sizes corresponding to the Cu(111) crystal plane were determined for each nanowire type. To find patterns differentiating the nanowire crystallinity, the crystallite sizes of each nanowire was calculated using the Scherrer equation, as shown in **Eq. 3** [61]

$$Crystallite\ size\ (D_{111}) = \left(\frac{\lambda \times K}{\beta \times \cos\theta}\right) \quad 3$$

Where, β = full width at half maximum (FWHM) (in radians); Scherrer's constant K = 0.94; λ = X-ray source wavelength = 0.15406 nm; θ = angle of diffraction.

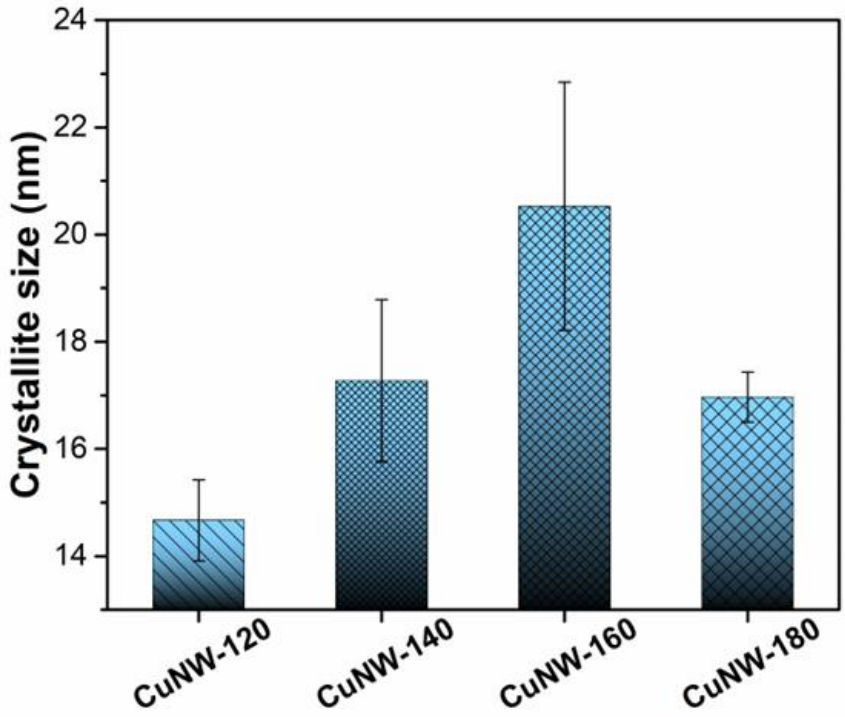

Figure 17: Bar plot showing crystallite size measured of CuNW-120, CuNW-140, CuNW-160 and CuNW-180. Adapted from [30].

The measured crystallite sizes were 15 ± 0.8, 17 ± 1.5, 21 ± 2.3, and 17 ± 0.5 nm, for CuNW-120, CuNW-140, CuNW-160, and CuNW-180, respectively (plotted in **Fig. 17)**. These results show that the crystallite size (D_{111}) increases from a lower value until it reaches a maximum for CuNW-160. Crystallite size plays a key role in the oxidation behaviour of a material. Smaller crystallite size results in a higher density of grain boundaries, which act as rapid diffusion pathways for oxygen [62]. As a result, oxidation tends to occur more readily along these boundaries than within the crystallites themselves, making them more susceptible to aerobic oxidation. Conversely, as crystallite size increases, the grain boundary density decreases, thereby decreasing the material's susceptibility to oxidation [62].

To gain deeper insight into the chemical composition and oxidation states of the nanowires, X-ray photoelectron spectroscopy (XPS) measurements were performed. The XPS survey spectra in **Fig. 18** show that copper (Cu), oxygen (O), and carbon (C) are the primary constituents of the nanowires. The presence of C and O can be attributed to the formation of a thin surface layer, which typically forms during the wet chemical synthesis of nanowires [31]. Additionally, a small amount of chlorine (Cl) was detected, which likely originates from the copper chloride precursor and may have adsorbed onto the surface of the nanowires.

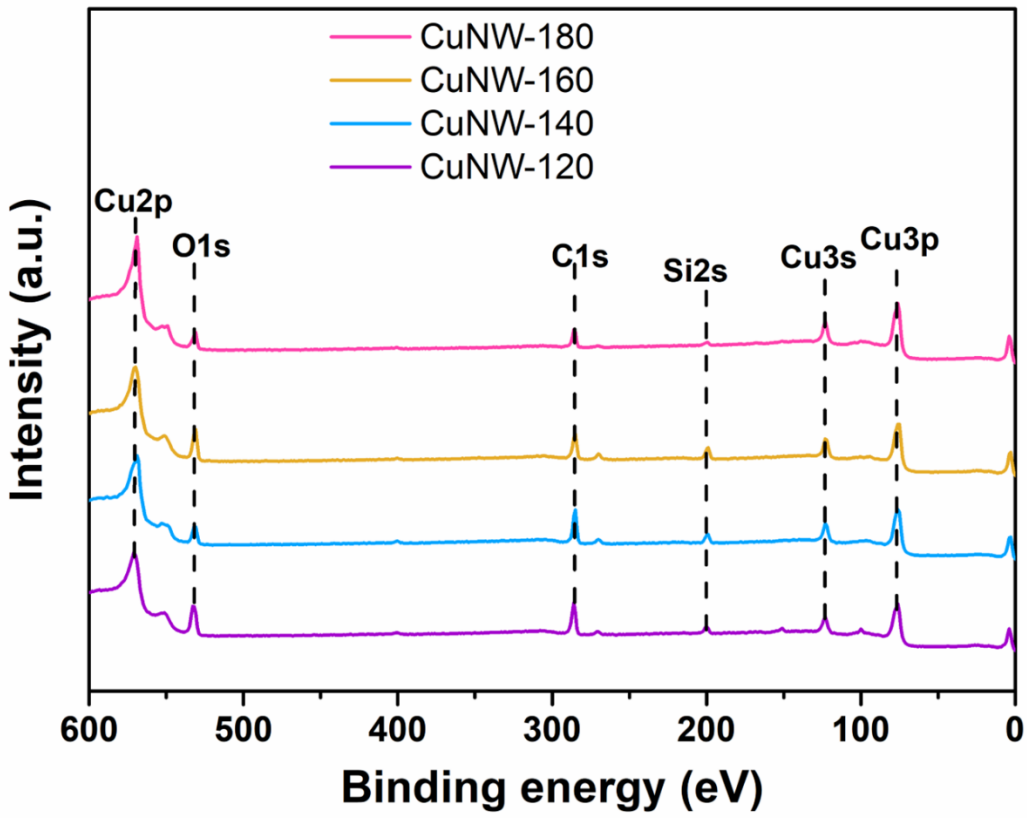

Figure 18: XPS survey spectra of CuNWs, adapted from [30].

High-resolution narrow scan spectra of Cu 2p (**Figure 19)** were obtained for each nanowire type to further investigate the surface chemistry of the nanowires. The spectrum for CuNW-120 exhibits a pronounced spin-orbit doublet in the range ~930–960 eV, with a separation of ~19.8 eV and an area ratio close to 2:1, which is characteristic of copper. Deconvolution of the spectrum reveals additional components at ~932.8 eV for Cu $2p_{3/2}$ and ~954.2 eV for Cu $2p_{1/2}$. These peaks shifted by ~1.4 eV relative to the Cu^0 peaks, indicating the presence of native surface oxides. This is further supported by the appearance of a shake-up satellite peak at ~939 - 948 eV [63]. Overall, the Cu 2p spectrum of CuNW-120 confirms the coexistence of metallic copper alongside oxidised copper species on the nanowires' surface. The Cu 2p spectra of CuNW-140, 160 and 180 show the characteristic spin-orbit doublet at ~932.8 eV for Cu $2p_{3/2}$ and ~954.2 eV for Cu $2p_{1/2}$, confirming that they are comprised fully of metallic copper directly after synthesis.

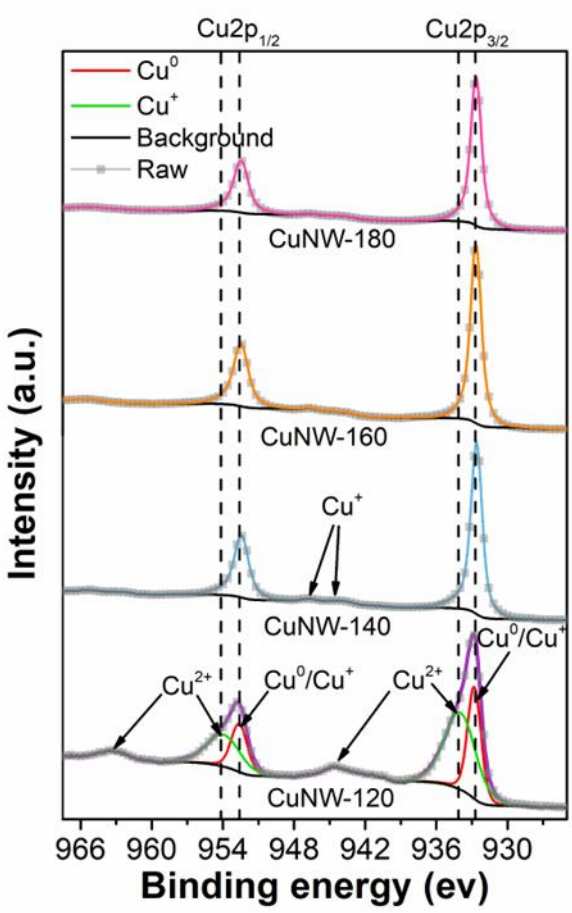

Figure 19: High-resolution narrow scan spectra of Cu 2p. Reproduced from [30].

The Cu LMM Auger spectra (**Figure 20**) provide further evidence for the coexistence of multiple copper oxidation states – Cu, Cu^{+} and Cu^{2+} – across all the nanowire types. This observation complements the Cu 2p spectra data. A clear trend is observed with increasing reaction temperature, namely, the amount of metallic copper (Cu^{0}) progressively increases. CuNW-120 exhibits the lowest fraction of Cu^{0}, indicating a comparatively higher degree of oxidation or incomplete reduction under lower synthesis temperature [55]. In contrast, CuNW-180 shows the highest Cu^{0} content among all the samples. This enhancement in metallic character can be attributed to higher temperature, which facilitates the more effective reduction of the copper salt precursor [64].

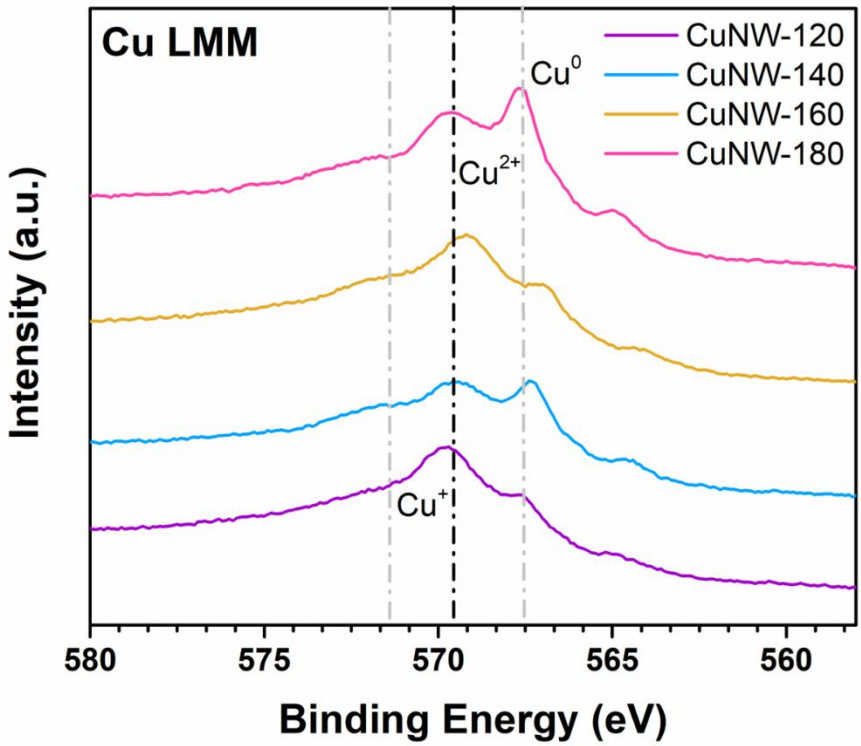

Figure 20: Cu LMM spectra of all CuNWs. Adapted from [30].

4.2 CuNW-PC film testing

Building on the morphological and surface chemistry analyses discussed above, the synthesised nanowires were utilised to investigate their functional properties in a device-relevant setup. For this purpose, copper nanowires (CuNWs) were assembled onto polycarbonate (PC)-based filter membranes using vacuum filtration [30]. This method enables the formation of percolated nanowire networks, which is well suited for analysing the electrical and physical properties of the nanowires accurately. As copper is highly reactive, especially at the nanoscale, and CuNWs tend to aggregate [65], it can be challenging to precisely evaluate their properties. By enabling swift assembly, vacuum filtration helps preserve the original dispersed state of nanowires before aggregation occurs. Therefore, we carefully selected this approach to fabricate CuNW-PC substrates for the evaluation of their properties. Using this method we prepared four CuNW-PC conductive substrates which were differentiated by their synthesis temperatures, CuNW-120-PC, CuNW-140-PC, CuNW-160-PC and CuNW-180-PC, respectively.

Typically, nanowires synthesised via solution-based approaches often develop surface oxide layers or are coated with organic residues from capping agents and solvents [31]. These surface

contaminants can significantly affect electrical conductivity. To address this issue, the CuNW-PC substrates were treated with propionic acid diluted in ethanol before analysis [38]. This treatment effectively removed surface oxides and organic residues, reducing sheet resistance from about 0.5-10 MΩ to about 9-30 Ω sq^{-1} [30].

4.2.1 Electrical conductivity over time

The electrical conductivity of metallic nanowire networks is affected by several key structural and surface-related parameters, such as nanowire diameter, length, crystallite size, surface oxides, and surface smoothness of the nanowires [23,25]. In general, nanowires with larger diameters and longer lengths enable more efficient electron transportation, as they provide a bigger conduction pathway [23]. Consequently, higher initial electrical conductivity is expected for CuNW-160 and CuNW-180. In contrast, nanowires with smaller diameters limit the number of electrons able to be transported and enhance surface-electron scattering, leading to increased resistance. This effect is particularly significant in thinner and rougher nanowires such as those in CuNW-120-PC [23].

Crystallite size also plays an important role in determining conductivity, as discussed earlier. For instance, as CuNW-160 exhibits the largest crystallite size, which reduces grain-boundary scattering and limits reactive sites for oxidative degradation [66]. This further enhances the expectation of superior conductivity from CuNW-160-PC.

Electrical conductivity is also controlled by the purity of the nanowire surfaces. From the XPS results, it was evident that the CuNW-120 was also composed of oxide layers, which increases the electrical sheet resistance [67]. Although CuNW-180-PC exhibits a smooth and less oxidised surface, its stability is compromised by broad distributions in nanowire length and diameter. This can weaken network percolation and increase junction resistance, ultimately limiting its electrical performance.

To evaluate the oxidation behaviour and long-term stability of the copper nanowire networks, the samples were stored under ambient conditions (25°C, ~35% relative humidity), and their electrical conductivity was monitored over a period of 60 days. Faster oxidation resulted in an increase in sheet resistance. To quantify this, the relative change in sheet resistance, $\Delta R/R_0$ was calculated using **Eq. 4** and tracked as a function of time **(Fig. 21)**. In **Eq. 4**, 'SR_0' and SR_i are the sheet resistances at the initial and i^{th} days. To account for spatial variations within the films, measurements were taken at five different positions on each CuNW-PC sample (n = 5), and the average values were used for analysis.

$$Relative\ sheet\ resistance\ \frac{\Delta R}{R^0} = \frac{SR_i - SR_0}{SR_0} \qquad 4$$

As shown in **Fig. 21** an increase in sheet resistance was observed for all nanowires over time, confirming progressive oxidation under ambient conditions. However, the extent of degradation varied significantly depending on the synthesis temperature of the nanowires. Conductive surfaces (CS) fabricated with CuNW-140 and CuNW-160 showed the best retention of conductivity, with $\Delta R/R_0$ values of only ~1.7 and ~1.8, respectively, after 60 days in ambient conditions. Notably, the $\Delta R/R_0$ values of CuNW-120 and CuNW-180 based CS were significantly higher than these, measuring as approximately 3.7 and 24 times higher than that of CuNW-160-PC. This highlights the superior oxidative stability of the CuNW-160-PC CS.

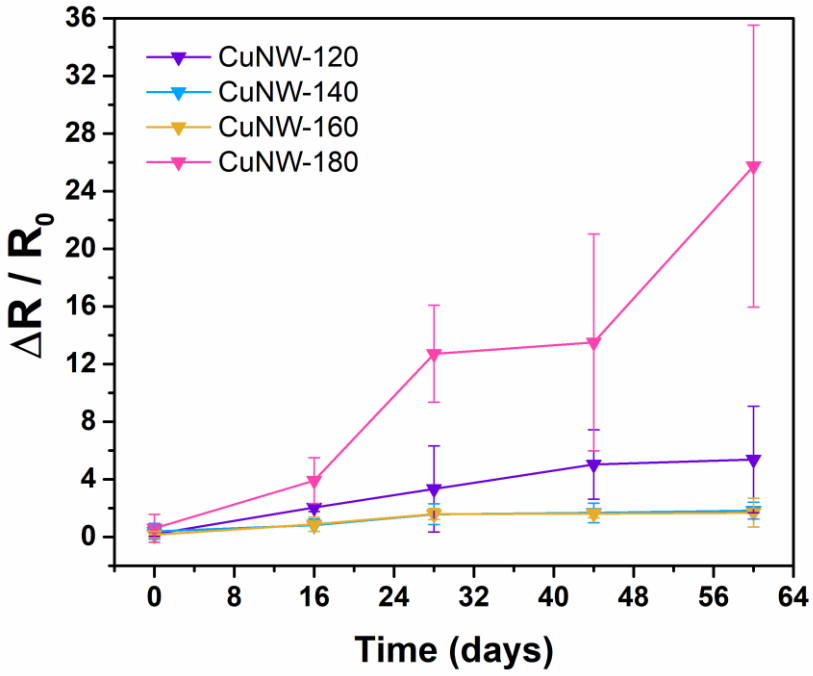

Figure 21: Relative sheet resistance over 60 days in ambient conditions (25°C, 35% RH). Reproduced from [30].

In addition to the electrical characterisation, visual changes in the CuNW-PC films were monitored as a qualitative indicator of oxidation. Colour change of the films was observed over 60 days, as certain kinds of colour change can indicate oxidation. As shown in **Fig. 22a**, the CuNW-120-PC film exhibited a light orange colour at 0 hours, characteristic of metallic copper. Already after 14 days the colour of the film had noticeably darkened (**Fig. 22b**), suggesting the onset of oxidation. After 60 days, the colour has greyed significantly (**Fig. 22c**), which is a sign of the formation of copper oxide species [39].

Figure 22: Colour change over time for CuNW-120-PC films **(a)** 0 hours **(b)** 14 days **(c)** 60 days.

Fig. 23 shows the colour change of CuNW-140-PC over a period of 60 days. At the initial stage (0 hours) the colour is a light orange (**Fig. 23a**), characteristic of metallic copper. Notably, no discernible change in colour is observed after 14 days (**Fig. 23b**), and the film retains a similar colour even after 60 days of exposure to ambient conditions (**Fig. 23c**). This stability in colour is consistent with the electrical measurements, which showed minimal variation in sheet resistance for CuNW-140_PC over time. The absence of significant colour change suggests that oxidation is either negligible or occurs at a very slow rate.

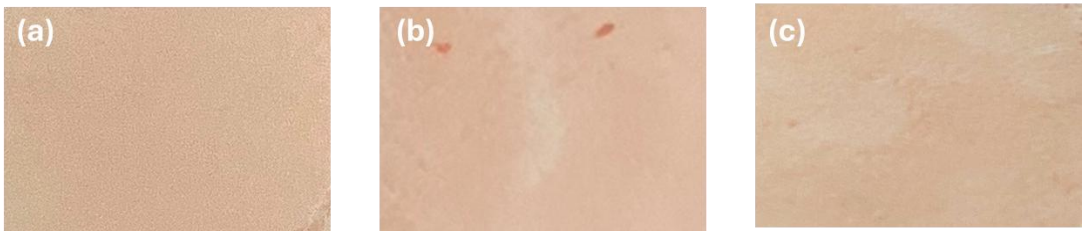

Figure 23: Colour change over time for CuNW-140-PC films **(a)** 0 hours **(b)** 14 days **(c)** 60 days.

Fig. 24 presents the colour change of CuNW-160-PC over 60 days in ambient conditions. At 0 hours the film displays a bright orange colour (**Fig. 24a**), indicative of metallic copper with minimal surface oxidation. Importantly, in both images after 14 days (**Fig. 24b**) and 60 days (**Fig. 24c**) no noticeable change in colour can be observed. The consistent colour of CuNW-160-PC strongly correlates with the sheet resistance measurements, which showed relative stability in conductivity over 60 days. This further confirms the excellent oxidative stability of CuNW-160-PC.

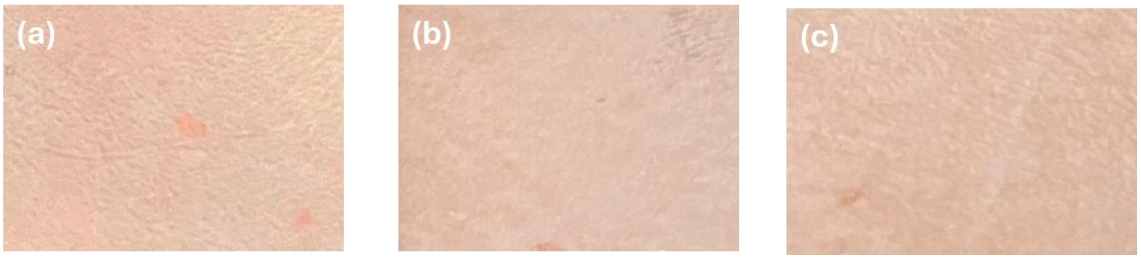

Figure 24: Colour change over time for CuNW-160-PC films **(a)** 0 hours **(b)** 14 days **(c)** 60 days.

Fig. 25 shows the colour change of the CuNW-180-PC over 60 days in ambient conditions. At the initial stage (0 hours) the colour of the film is a light orange (**Fig. 25a**), characteristic of metallic copper. However, already after 14 days the colour of the film has noticeably darkened (**Fig. 25b**), indicating surface oxidation. After 60 days, the film's colour has further darkened, especially in the spot on the top right (**Fig. 25c**), which suggests localised oxidation. Such changes in colour can be associated with copper oxide formation [39]. These observations are consistent with the progressive oxidation of CuNW-180-PC noted from the sheet resistance measurements, highlighting the poor stability of CuNW-180-PC in ambient conditions.

Figure 25: Colour change over time for CuNW-180-PC films **(a)** 0 hours **(b)** 14 days **(c)** 60 days.

To gain further insights into the oxidation behaviour of the different nanowires, X-ray photoelectron spectroscopy (XPS) was performed after 28 days as shown in **Figure 26**. The spectrum revealed the evolution of Cu 3p spin-orbit doublet peaks ($3p_{3/2}$ and $3p_{1/2}$), progressively shifting toward higher binding energies over time. This shift is indicative of the formation of CuO on the nanowire surface. This confirms that the reduction in electrical conductivity was due to the gradual oxidation of conductive Cu^0 to semiconducting CuO nanowires.

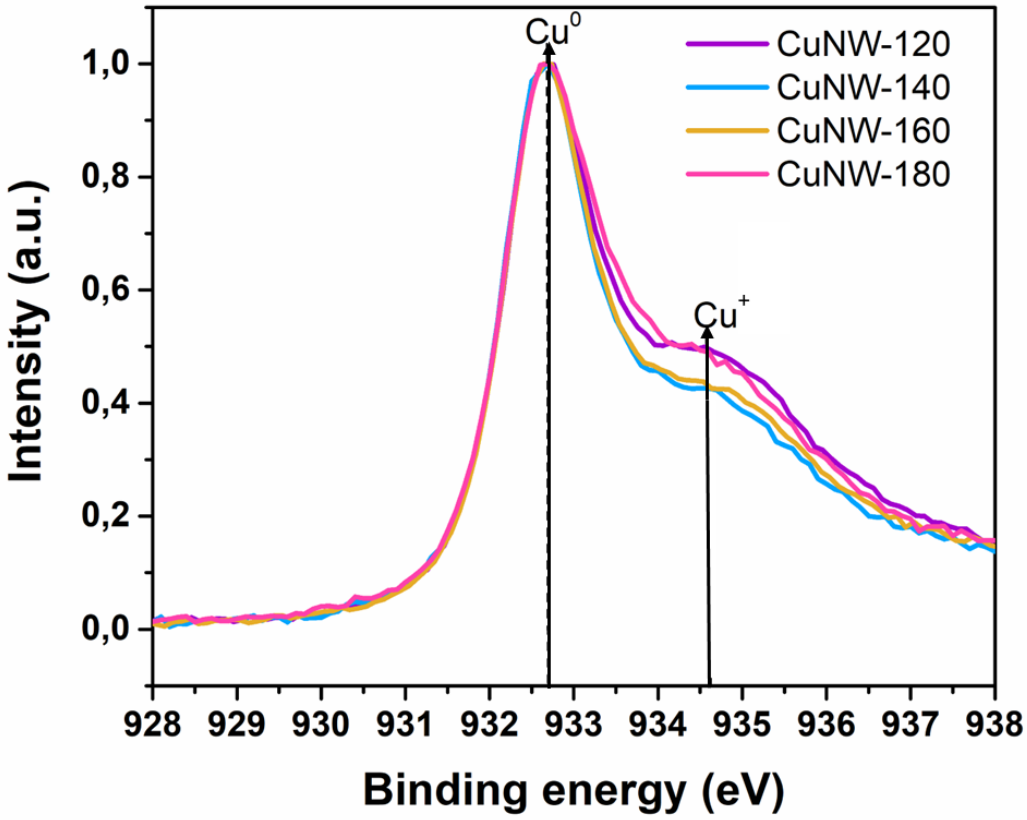

Figure 26: XPS spectra after 28 days, adapted from [30].

4.2.2 Mechanical durability

Flexibility tests were performed to assess the mechanical properties of the CuNW-PC conductive films. In this context, flexibility is defined by the extent to which the CuNW-PC substrate can withstand bending without any significant loss in resistance. This was quantitatively evaluated by measuring resistance as a function of curvature using a texture analyser in combination with an LCR meter. The curvature was first obtained for the CuNW-140-PC substrate, as shown in **Fig. 27**. All CuNW-PC surfaces were then subjected to bending within a curvature range of 124–489 m^{-1}. Across this range, all the nanowire-based conductive surfaces maintained low sheet resistance, demonstrating their potential for flexible electronic applications. CuNW-160-PC exhibited the most stable electrical performance under bending. Even at the maximum curvature of 489 m^{-1}, the resistance increased by only 0.6 Ω. Similar behaviour was exhibited by the other CuNW samples, as can be seen in the plot in **Fig. 28**.

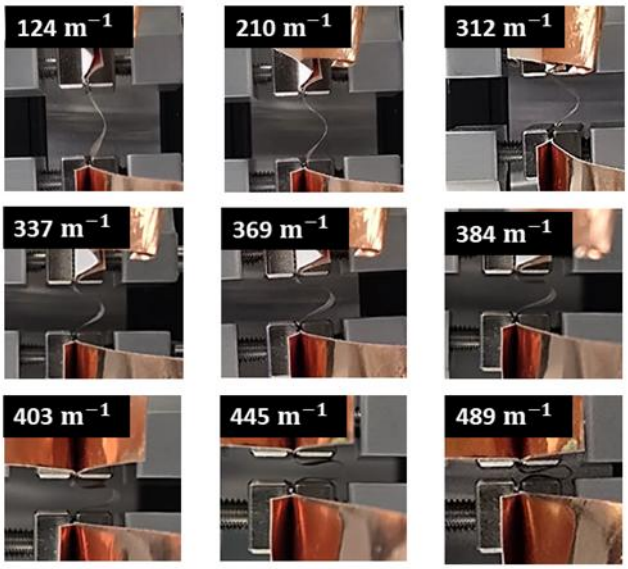

Figure 27: Curvature measured from CuNW-140-PC, reproduced from [30].

CuNW-180-PC also showed relatively low sensitivity to bending, however, it exhibited a higher initial resistance compared to CuNW-160-PC. In contrast, CuNW-120-PC displayed significantly higher initial resistance and a pronounced increase in resistance beyond a curvature of ~369 m^{-1}. Similarly to CuNW-160-PC, CuNW-140-PC maintained stable performance until ~445 m^{-1}, after which a noticeable increase in resistance was observed. This behaviour is consistent with strain-induced junction failure. The deviation from the usual "thinner-is-more-flexible" expectation likely arises due to differences in junction quality, surface smoothness, and emerging oxidation (particularly in CuNW-120), which elevate intrinsic and contact resistances under bending [68].

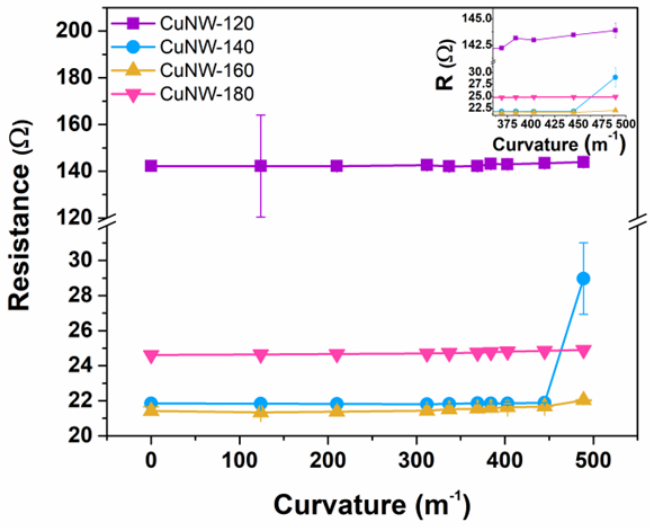

Figure 28: Curvature VS Resistance for CuNW-120, 140, 160 and 180, reproduced from [30].

4.2.3 Stability after humidity treatment

The stability of the nanowire-PC surfaces under elevated humidity was investigated by placing samples in a weathering chamber at 25 °C and 85% relative humidity (RH). The change in electrical performance was evaluated by monitoring the relative change in sheet resistance ($\Delta R/R_0$) over a period of 16 days (**Fig. 29**). After exposure period, $\Delta R/R_0$ values of 3.4, 1.7, 2.2, and 6.8 were recorded for CuNW-120, CuNW-140, CuNW-160, and CuNW-180, respectively. Among the samples, CuNW-120-PC and CuNW-180-PC exhibited significant increases in sheet resistance indicating moisture-induced degradation. In contrast, CuNW-140-PC and CuNW-160-PC, exhibited only minimal changes in sheet resistance, demonstrating that the nanowires synthesised at 140 and 160 °C remained largely intact after prolonged exposure to humidity. These nanowires maintained high stability, approaching that of encapsulated systems, demonstrating performance competitive with current literature [69].

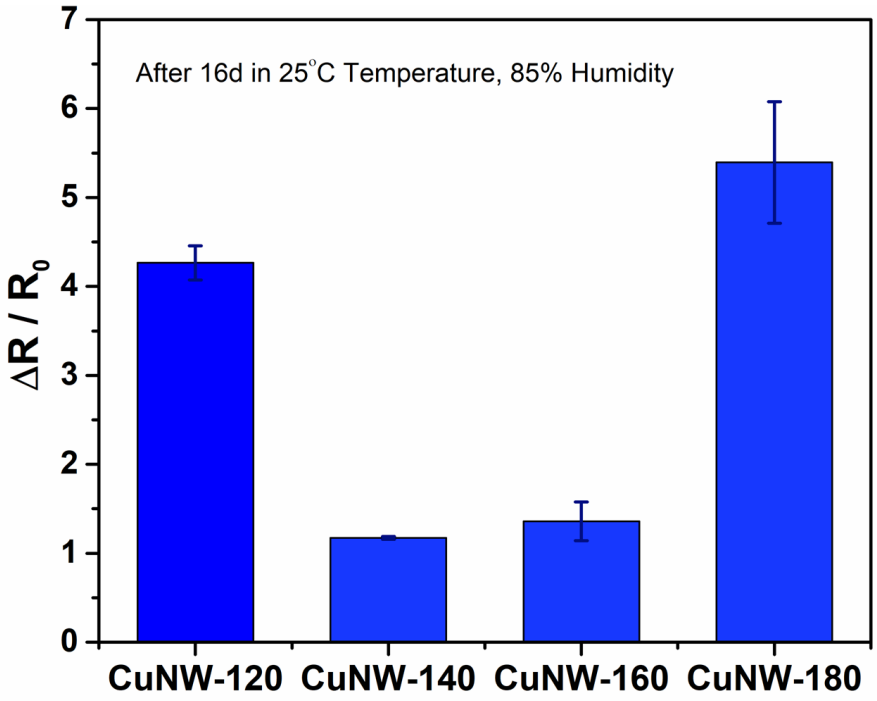

Figure 29: Relative sheet resistance changes of CuNW-PC films after 16 days in a weather chamber set at 25°C and 85% relative humidity. Adapted from [30].

These observations further support the earlier observed trend of conductivity degradation observed in ambient conditions (**Fig. 21**). Consistent with these findings, the CuNW-160 and CuNW-140 surfaces maintained their conductivity the best, , while the CuNW-180 and CuNW-120 surfaces degraded the most, with much more pronounced decreases in conductivity.

Following the humidity exposure test, the CuNW-PC surfaces were subjected to 10,000 bending cycles, after which they were stored in ambient conditions for ~1 month. SEM imaging revealed that nanowire morphology remained largely unchanged over this period (**Fig. 30 a, c, e, g**), indicating that mechanical deformation and short-term storage in ambient conditions did not disturb the nanowire networks. However, after ~3 months of storage in ambient conditions, noticeable morphological changes became apparent in the CuNW-120 nanowires (**Fig. 30 b**). In contrast, the nanowires on the CuNW-140-PC, CuNW-160-PC, and CuNW-180-PC surfaces showed little to no structural alterations (**Fig. 30 d, f, h**). This indicates that CuNW-120 is more susceptible to oxidative degradation than the nanowires synthesised at 140, 160 and 180 °C.

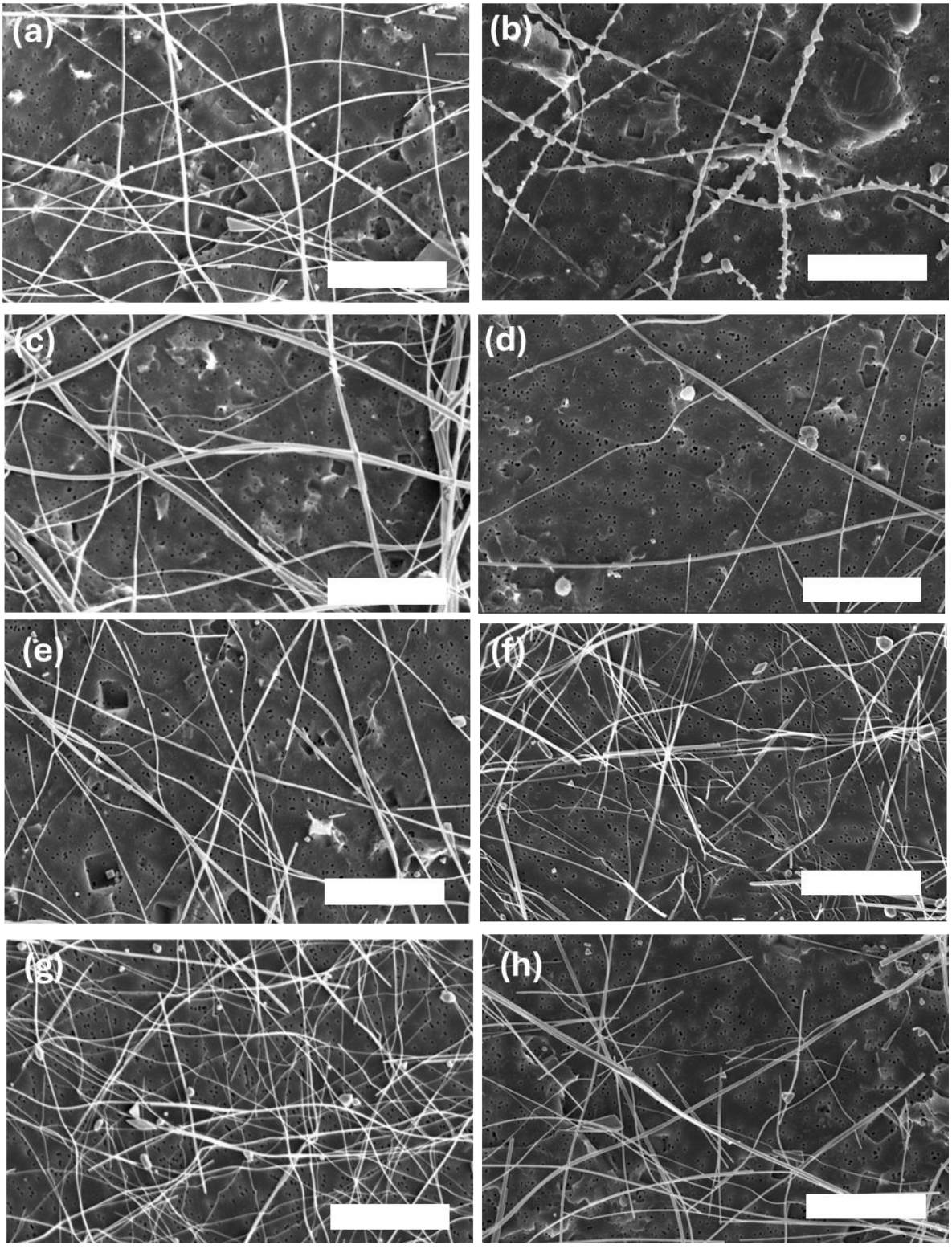

Figure 30: SEM images of CuNW-PC surfaces after being stored in a weather chamber at relative humidity 85% and temperature 25°C for 16 days, followed by 10,000 bending cycles, scale bar 5 μm. Adapted from [30]. SEM images acquired within 1-month post-exposure: **(a)** CuNW-120, **(c)** CuNW-140, **(e)** CuNW-160, **(g)** CuNW-180. SEM images acquired within 3 months post-exposure: **(b)** CuNW-120, **(d)** CuNW-140, **(f)** CuNW-160, **(h)** CuNW-180.

4.2.4 Thermal and electrical durability

Thermal stability of the CuNW-PC substrates was also systematically evaluated to assess their performance over a range of 20 °C to 140 °C, as shown in **Fig. 31**. Initially at lower temperatures, CuNW-120-PC shows relatively low resistance. However, a clear increase in resistance is observed beyond, ~60 °C, suggesting the start of thermally induced degradation. In contrast, CuNW-160-PC exhibited the highest thermal stability among all samples, confirming that nanowires synthesised at higher reaction temperatures demonstrate enhanced performance and stability.

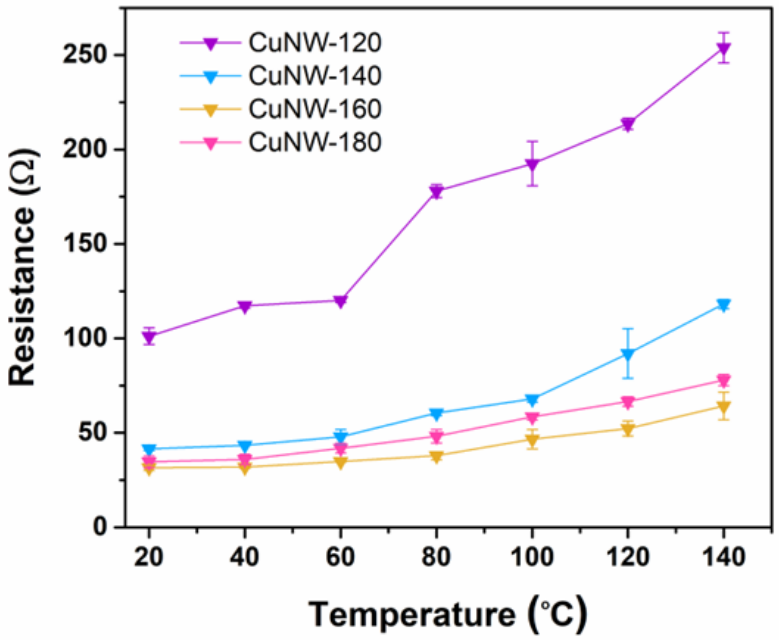

Figure 31: Temperature VS Resistance plot for CuNW-PC surfaces. Reproduced from [30].

Thermal degradation can be attributed to a combination of thermally activated degradation mechanisms. One key factor is Rayleigh (capillary) instability, which drives nanowire spheroidization, where nanowires break up into isolated segments, disrupting conductive pathways [70]. Thermal oxidation is another thermally activated degradation mechanism, which often co-occurs with Rayleigh instability, intensifying degradation. Additionally, the thermal behaviour of the underlying polycarbonate (PC) substrate must be considered. At higher temperatures, thermal softening of the PC substrate can occur, which could promote nanowire rearrangement and subsequently lead to increased oxidation [71].

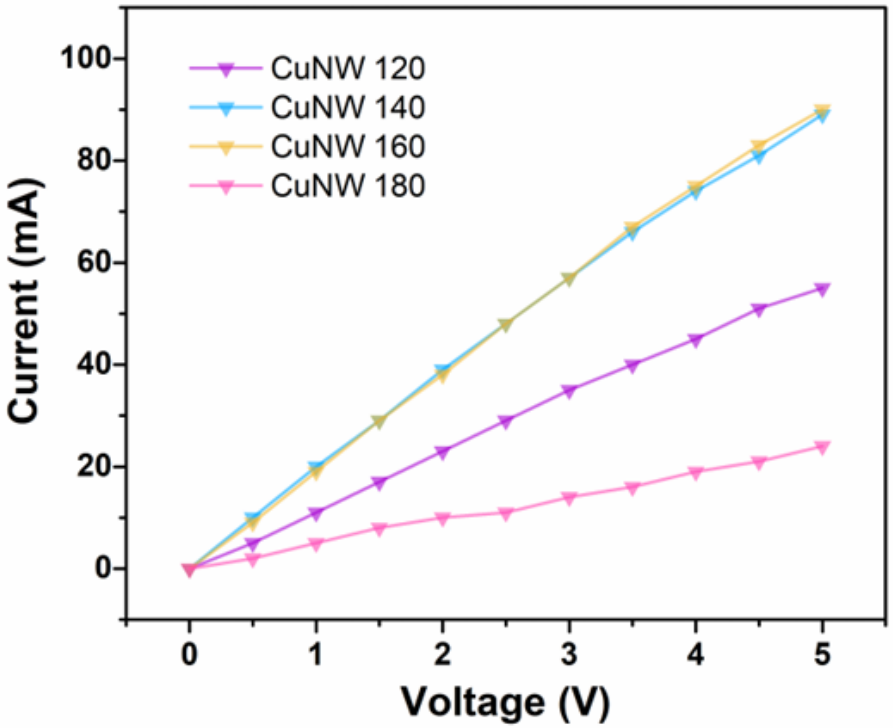

Figure 32: I-V plot for CuNW-PC surfaces. Reproduced from [30].

The electrical robustness and charge transport behaviour of the CuNW-PC films were investigated using current-voltage (I-V) measurements, as presented in **Fig. 32**. All the nanowire-PC surfaces exhibit a linear I-V response over the applied voltage range (0-5 V), confirming their behaviour as ohmic conductors. A clear variation in electrical performance is observed between different samples, with the electrical conductivity trend following the order: CuNW-160 ~ CuNW-140 >> CuNW-120 >> CuNW-180. The CuNW-180-PC film shows the lowest slope in the I-V curve, corresponding to reduced conductivity with more voltage applied. This behaviour is likely associated with less effective nanowire network formation, potentially due to shorter or less uniform nanowires that reduce parallel conduction paths. The CuNW-120-PC shows intermediate performance, with a slightly steeper IV-curve slope than that of CuNW-180-PC. However, its conductivity is still notably lower than that of CuNW-140 and CuNW-160. This can be due to a combination of higher intrinsic and junction resistance. As indicated by XPS analysis, the presence of surface oxide layers on CuNW-120 introduces insulating barriers at the nanowire interfaces, which elevates junction resistance.

The CuNW-140-PC and CuNW-160-PC samples demonstrate the highest current response across the entire voltage range, reflecting their superior electrical conductivity. This is caused by longer nanowires forming well-percolated nanowire networks with efficient inter-nanowire junctions.

Moreover, these samples maintain linear IV-character even at high voltage, which suggests that the nanowire networks are stable under increased electrical stress.

4.2.5 Stability comparison with other CuNW coated surfaces

To further evaluate the stability of our nanowire-PC surfaces, a detailed comparison was conducted with previous reports in the literature (**Tab. 2**). In general, copper nanowires synthesised using similar wet-chemical methods show poorer long-term conductivity on flexible substrates than our CuNW-160-PC. Multiple studies using uncoated CuNWs for FCS showed both higher relative sheet resistance changes ($\Delta R / R_0$) over time and shorter operational lifetimes than CuNW-160-PC. For instance, studies by Yu et al., Tran et al., Rathmell et al. and Yin et al. reported that CuNW FCS retained conductivity for only 2, 4, 7, and 28 days, respectively [39,40,57,72]. These results indicate rapid nanowire network degradation, primarily due to rapid oxidation in air, a key flaw of copper nanowires.

Table 2: Stability comparison of various copper nanowire coated surfaces from literature from the past 15 years. Reproduced from [30].

Type of nanowires	Nanowires	Synthesis Temperature (°C)	Reaction Time (h)	$\Delta R / R_0$	Stability* (days)	References
Naked nanowires	CuNW-160	160	4	~1.7	>60	[30]
	CuNWs	180	12	0.4	50	[73]
	CuNW ink	80	1	~0.5	42	[74]
	CuNWs	260 (preheat at 110 °C, 0.5 h)	30 min	~1.1	38	[75]
	CuNWs	80	1	~9.7	28	[72]
	CuNW	198 (preheat at 110 °C, 0.5 h)	1	~3	7	[57]
	CuNWs	100	7	~20	4	[39]
	CuNWs	120	20	~3	2	[40]
Encapsulated nanowires	CuNWs sandwiched in PES / PET	110	12	~1	45	[76]
	CuNW@Au core-shell NWs	165	18	~1	~40	[36]
	TiO_2 coated CuNWs	100	7	~2	30	[39]
	CuNW conductive tape	120	20	~2	7	[40]

*Stability at ambient conditions, 25 °C and ~35% humidity

While some studies showed lower $\Delta R / R_0$ changes over time than that of CuNW-160, their stability duration, however, remained lower than that of our CuNWs. For example, Chu et al. fabricated FCS using uncoated CuNWs, which showed an $\Delta R / R_0$ change of ~1.1 after 38 days [75], which is less than the ~1.7 of CuNW-160. As 38 days is still significantly shorter than 60 days, it can be concluded that CuNW-160 outperformed this CuNW FCS in terms of stability. This highlights that both resistance change and duration of stability must be considered when evaluating the performance of FCS.

Notably, CuNW-160-PC also demonstrates performance comparable to, and in some cases exceeding that of, oxidation-protected CuNW-based FCS. This is significant as CuNW-160-PC uses nanowires with no additional protective coating or encapsulation. For instance, CuNW-based conductive tape and CuNW FCS coated with titanium oxide exhibited shorter lifetimes of only 7 and 30 days, respectively [39,40]. These durations of stability are significantly shorter than the 60 days of our uncoated nanowire surfaces. Overall, CuNW-160-PC demonstrates superior ambient stability when compared to both coated and uncoated CuNW FCS. This highlights the strong potential of the nanowires for application in durable flexible sensors.

4.3 Curvature sensor application

The CuNW-N-6 surface is highly flexible, which makes it suitable for use in capacitive curvature sensors. To create a capacitive curvature sensor, we used two pieces of CuNW-N-6 film as the conductive part of the sensor and a clean piece of N-6 film as the dielectric layer [30]. To evaluate the CuNW-N-6 curvature sensor's performance, it was clamped at its edges and bent 10,000 times to maximum bending radius using a texture analyser while measuring the curvature (using a digital camera and Image J) and the change in capacitance (using an LCR meter).

CuNWs possess high surface energy, which promotes rapid agglomeration and thus degrades electrical conductivity. To mitigate agglomeration, we employed electrospun N-6 nanofibre surfaces as flexible substrates [77]. Electrospun nanofibres are continuous ultralong polymeric fibres with micro- to nanometre-scale diameters. Highly rough and porous surfaces of the nanofibre mesh are permeable to air and liquids, which make them suitable surfaces for depositing nanowires, avoiding agglomeration for high-performance flexible sensors [78]. Accordingly, CuNW suspensions were deposited onto the N-6 nanofibre surface by vacuum filtration, which enabled rapid and uniform loading of nanowires. This approach suppresses aggregation and produces compact and percolated conductive nanowire networks. Hereafter, this nanowire-N-6 nanofibre surface will be referred to as flexible conducting surfaces (FCS). Further, the FCS was analysed using SEM. The identities of the

nanowires and N-6 nanofibres are clearly distinguishable in the backscattered electron detector. Nanowires appeared with bright lines at the forefront, while nanofibres appeared with a grey background. To analyse the elemental composition of the FCS, energy dispersive X-ray spectroscopy (EDS) was used as shown in **Fig. 33 a-d**. As expected, carbon, nitrogen, and oxygen were present in the N-6 nanofibres, and copper was present in the nanowires, indicating effective integration of CuNWs onto the N-6 nanofibre surface.

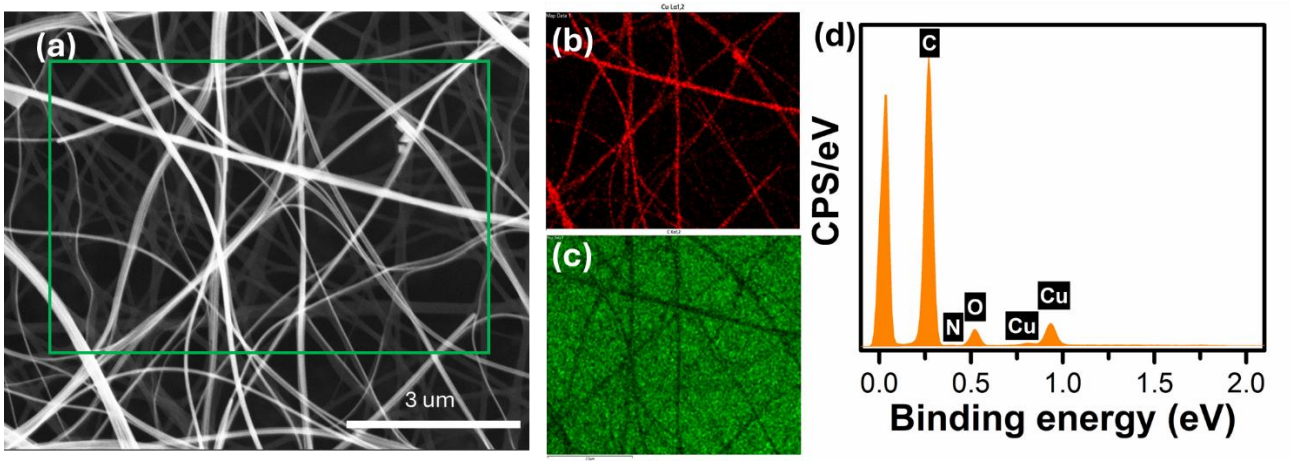

Figure 33: SEM analysis of CuNW-160-N-6 FCS **(a)** SEM micrograph with EDS elemental mapping overlay area in the green box **(b)** Cu from nanowires shown in red **(c)** N from Nylon-6 shown in green **(d)** EDS spectrum of elemental mapping overlay area. Reproduced from [30].

An electrospun N-6 nanofibre surface served as the dielectric layer in the flexible capacitive curvature sensor. An insulating layer is required to prevent the short-circuiting of the sensor, which is why an N-6 nanofibre was sandwiched between two conducting FCS. To test its performance, the device was subjected to bending while the relative capacitance change ($\Delta C/C_0$) was recorded. The recording of $\Delta C/C_0$ was conducted using an integrated system consisting of a texture analyser, LCR meter and MATLAB. As the distance between the two FCS in the active region changes, the sensor responds with a change in capacitance. This response follows the parallel plate capacitance equation as displayed in **Eq. 5** [79].

$$Capacitance\ (C) = \left(\frac{\varepsilon \times A}{d}\right) \quad \textbf{5}$$

Where, C = capacitance in Farads, ε = permittivity of dielectric medium, A = area of the active region in square meters and d = distance between the electrode surfaces in meters.

Each fabricated sensors were subjected to 10,000 bending cycles directly after fabrication. The development of the $\Delta C/C_0$ signals for each sensor over the testing period is illustrated in **Fig. 34**. At

the beginning of the testing, the sensors all exhibited strong $\Delta C/C_0$ signals under bending. Based on the plot shown in **Fig. 34**, the sensors based on CuNW-160-N-6 and CuNW-140-N-6 exhibited the most stable response over 10000 bending cycles. Their $\Delta C/C_0$ signal remained constant with negligible noise, which is a sign of a durable nanowire network.

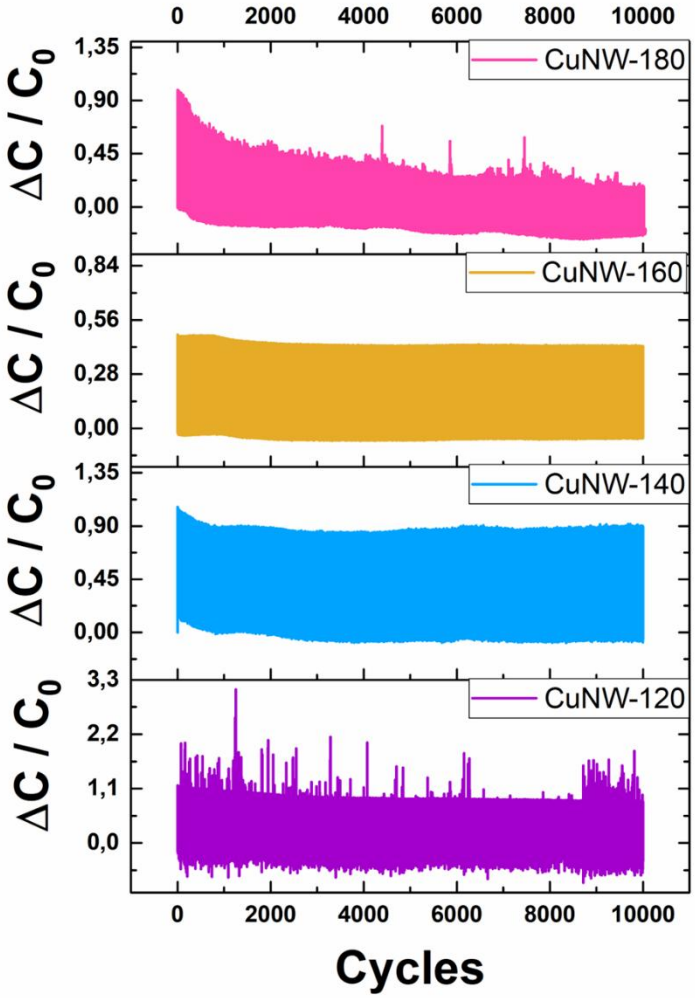

Figure 34: Capacitance change over 10000 cycles for sensors based on nanowires synthesised at different temperatures. Adapted from [30].

In contrast, the sensor containing CuNW-180-N-6 FCS showed a gradual decay of $\Delta C/C_0$ signal over the first several thousand cycles (**Fig. 34**). Additionally transient spikes can be observed from the **Fig. 34** plot around 4000 and 6000 cycles, possibly due to evolving interfacial slip or microcrack formation. Expanded plots of the cycles 990-1000 and 5990-6000 are shown in **Fig. 35**, further indicating the degradation of the signals of the CuNW-180-N-6 based sensor. The flattening curve of the $\Delta C/C_0$ signal at 5990-6000 cycles indicates lessened curvature sensitivity. Meanwhile, the sensor using CuNW-120-N-6 FCS exhibited comparatively higher curvature sensitivity but also showed

highly irregular and noisy response throughout the 10000 bending cycles (in **Figs. 34** and **35**). This implies irregular nanowire junctions leading to junction failure and unreliable sensing behaviour, despite the larger $\Delta C/C_0$ value. In conclusion, the bending-durability ranking after the 10,000 cyclic bending test was determined as CuNW-160 ≥ CuNW-140 >> CuNW-180 > CuNW-120, with CuNW-160 and CuNW-140 based sensors offering the most favourable combination of stability and reliability.

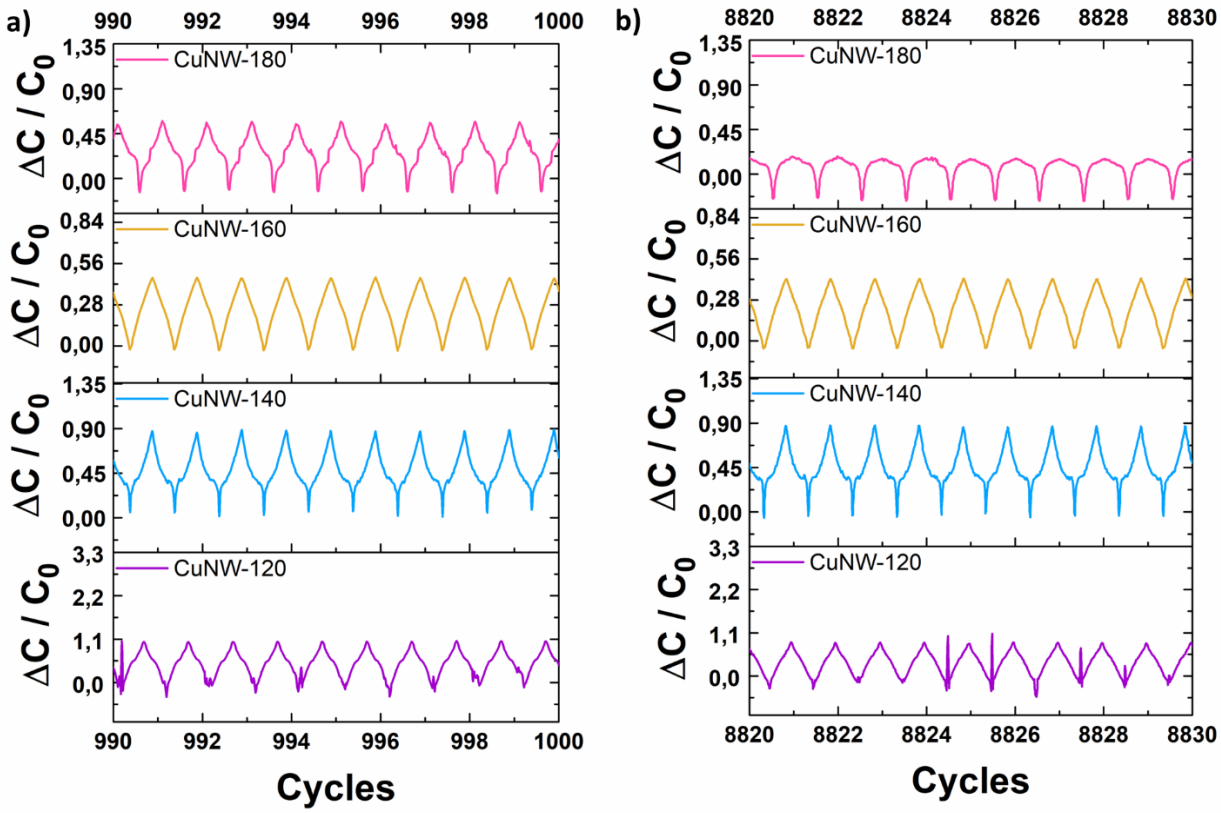

Figure 35: $\Delta C/C_0$ vs. bending cycles for durability tests under 10,000 bending cycles for CuNW-N-6 sensors [30], **(a)** magnified to cycles 990-1000 and **(b)** 8820-8830.

The curvature response was also analysed after storing the sensors in ambient conditions. **Fig. 36** presents the normalised capacitance change ($\Delta C/C_0$) as a function of curvature (κ) in the range of 0 to 450 m^{-1}. At the initial measurement (0 hours), the CuNW-140 and CuNW-160 based sensors exhibited a near linear $\Delta C/C_0$ — κ relationship across the tested curvature range, which is a sign of high-quality curvature sensitivity. After 75 days of storage, the linearity of the signal for these sensors remained largely intact, with only a small drop in sensitivity, demonstrating excellent stability in ambient conditions. The CuNW-180 based sensor shows a moderate, nonlinear initial response. However, it exhibited a substantial decrease in sensitivity within 14 days (**Fig. 36**), which aligns with the sensitivity degradation and transient spikes observed during the cyclic testing (**Fig. 35**) [30]. The

CuNW-120 based sensor displayed the highest initial curvature sensitivity, but as observed from Fig. 35, over multiple cycles its response is clearly nonlinear. This reflects a highly compressible electrode network [30]. After 14 days, the $\Delta C/C_0$ response remained higher than that of the sensors based on the nanowires prepared at other temperature; however, its sensitivity still decreased relative to its initial value. When considered with its noisy behaviour under cyclic bending, this indicates a clear improvement in responsiveness but lower reliability for accurate sensing measurements.

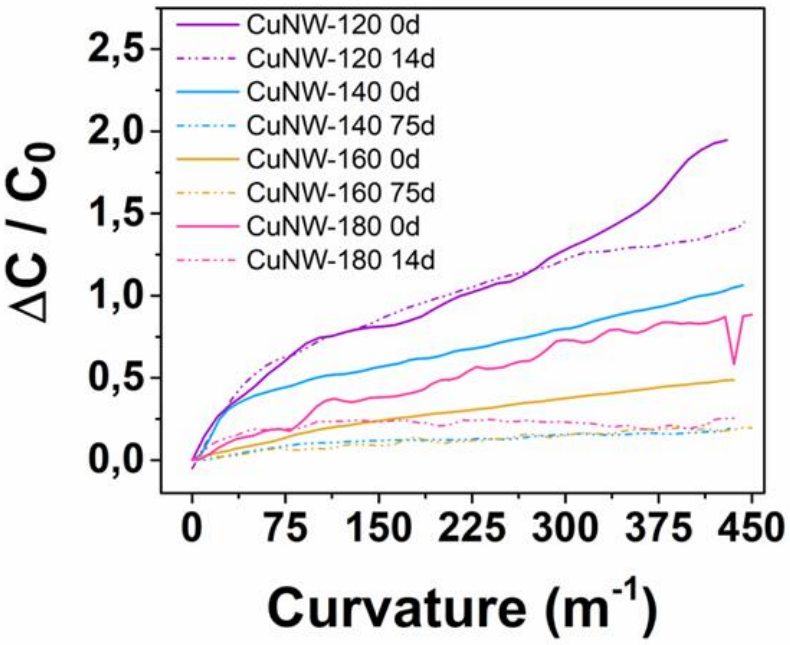

Figure 36: Curvature sensitivity comparison at 0h and after some time (14d / 75d). Adapted from [30].

Overall, for practical application and reliable curvature sensing, the CuNW-160 and CuNW-140 sensors demonstrate the most balanced performance. These devices combine mechanical durability and stable response, maintaining near-linear sensitivity. In addition, both sensors retain these sensing characteristics over extended ageing. This indicates that the CuNW percolation networks in the FCS remain intact, which supports their potential for application in devices. In direct contrast to the CuNW-160 and CuNW-140 sensors, the CuNW-180 sensor showed significantly lower mechanical durability as well as ageing-related loss of sensitivity. This suggests an unstable nanowire network and weakened junction contact between the nanowires. Finally, the CuNW-120 sensor, despite high sensitivity, is hindered by its pronounced noise and signal irregularity. As a result, it would be difficult to apply in devices due to the lack of a reliable response and increased need of noise filtration.

5 Conclusions

In this thesis, ultra-long copper nanowires (CuNWs) were successfully synthesised at reaction temperatures of 120 °C, 140 °C, 160 °C and 180 °C, yielding length-to-diameter aspect ratios of 558, 1356, 1939, and 865, respectively. A comprehensive structural, chemical and morphological characterisation revealed a clear correlation of nanowire properties and synthesis temperature. Nanowires synthesised at lower temperatures (e.g. 120 °C) were comparatively shorter, thinner, had smaller crystallite size and exhibited rougher surfaces with more pronounced oxide layers. In contrast, increasing the synthesis temperature led to the formation of longer, thicker nanowires with larger crystallite size, smoother surfaces and reduced oxide layers (e.g. 160 °C). However, at the highest reaction temperature tested (~180 °C), structural and morphological irregularities emerged, due to the thermal decomposition of the capping agents oleylamine and oleic acid.

To evaluate functional properties, CuNWs were assembled into conductive networks onto polycarbonate (PC) substrates, on which electrical, thermal and mechanical testing was conducted. The results of the CuNW-PC substrate testing showed a clear connection to synthesis temperature. Among all the samples, CuNW-160-PC exhibited the best overall performance (e.g. relative change in sheet resistance after 60 days: ~1.7, stable electrical performance up to 140 °C). CuNW-140-PC demonstrated the second-best performance, while CuNW-180 and CuNW-120 showed comparatively poorer stability. CuNW-140 and CuNW-160 films outperformed the other samples in stability under high humidity (85% RH). This trend was consistent across the performance metrics studied, including long-term oxidation stability, resistance under bending, thermal durability and electrical durability.

Device applicability of the nanowires was assessed by fabricating curvature sensors using flexible conducting surfaces based on electrospun nylon-6 nanofibre surfaces and CuNWs. After 10,000 bending cycles and studying curvature sensitivity decline over time, CuNW-160 and CuNW-140 based sensors offered the best option for device application, as they proved to have stable and near-linear sensitivity that persevered after extended ageing. Directly on the contrary, the CuNW-180 based sensor showed rapid loss of sensitivity over time. The CuNW-120 based sensor was not considered recommendable for practical application despite its high curvature sensitivity, as its signals display nonlinearity and unreliable dynamics.

In conclusion, the most suitable synthesis temperatures (in °C) follow the order $120 < 180 \ll 140 \leq 160$ for application in flexible sensors. Copper nanowires are prone to rapid oxidation, which has limited their adoption in flexible electronics. These results demonstrate that by optimising the

synthesis temperature of CuNWs, better stability of performance can be obtained, which addresses a major bottleneck in the research of replacing AgNWs with CuNWs in flexible electronics research.

Acknowledgements

I am grateful to the Materials Engineering Unit at the University of Turku and especially the Materials for Flexible Devices research group for providing me the opportunity to perform this research.

Big thanks to everyone who helped in the characterisation of the copper nanowires: Sari Granroth for X-ray photoelectron spectroscopy measurements, Ermei Mäkilä for assistance in scanning electron microscopy, Nidhin Mathews for TEM analysis and Rituporn Gogoi for SEM analysis. Thank you to Amit Barua and Shaharyar Siddique for support in the device fabrication and mechanical durability analysis of the CuNWs. I would like to also thank my supervisors, Vipul Sharma and Rituporn Gogoi for their guidance and reviewing this work.

References

[1] Y. Yuan, B. Liu, H. Li, M. Li, Y. Song, R. Wang, T. Wang, H. Zhang, Flexible Wearable Sensors in Medical Monitoring, Biosensors (Basel). 12 (2022). https://doi.org/10.3390/bios12121069.

[2] S. Zhao, F. Han, J. Li, X. Meng, W. Huang, D. Cao, G. Zhang, R. Sun, C.P. Wong, Advancements in Copper Nanowires: Synthesis, Purification, Assemblies, Surface Modification, and Applications, Small 14 (2018). https://doi.org/10.1002/smll.201800047.

[3] V.B. Nam, D. Lee, Copper nanowires and their applications for flexible, transparent conducting films: A review, Nanomaterials 6 (2016). https://doi.org/10.3390/nano6030047.

[4] J.S. Meena, S. Bin Choi, S.B. Jung, J.W. Kim, Electronic textiles: New age of wearable technology for healthcare and fitness solutions, Mater. Today Bio 19 (2023). https://doi.org/10.1016/j.mtbio.2023.100565.

[5] S.U. Zaman, X. Tao, C. Cochrane, V. Koncar, Smart e-textile systems: A review for healthcare applications, Electronics (Switzerland) 11 (2022). https://doi.org/10.3390/electronics11010099.

[6] G. Verma, S. Sarma, E. Koch, A. Dietzel, Flexible touch and gesture recognition system for curved surfaces with machine learning for assistive applications, Sensors and Actuators Reports 9 (2025). https://doi.org/10.1016/j.snr.2025.100284.

[7] S. Zhang, N. Nguyen, B. Leonhardt, C. Jolowsky, A. Hao, J.G. Park, R. Liang, Carbon-Nanotube-Based Electrical Conductors: Fabrication, Optimization, and Applications, Adv. Electron. Mater. 5 (2019). https://doi.org/10.1002/aelm.201800811.

[8] A. Kamyshny, S. Magdassi, Conductive nanomaterials for printed electronics, Small 10 (2014) 3515–3535. https://doi.org/10.1002/smll.201303000.

[9] J. Jiu, K. Suganuma, Metallic nanowires and their application, IEEE Trans. Compon. Packaging Manuf. Technol. 6 (2016) 1733–1751. https://doi.org/10.1109/TCPMT.2016.2581829.

[10] A. Razaq, F. Bibi, X. Zheng, R. Papadakis, S.H.M. Jafri, H. Li, Review on Graphene-, Graphene Oxide-, Reduced Graphene Oxide-Based Flexible Composites: From Fabrication to Applications, Materials 15 (2022). https://doi.org/10.3390/ma15031012.

[11] J. Ouyang, Application of intrinsically conducting polymers in flexible electronics, SmartMat 2 (2021) 263–285. https://doi.org/10.1002/smm2.1059.

[12] L. Yang, Y. Wu, F. Yang, W. Wang, A conductive polymer composed of a cellulose-based flexible film and carbon nanotubes, RSC Adv. 11 (2021) 20081–20088. https://doi.org/10.1039/d1ra03474j.

[13] Y. Yan, Y. Jiang, E.L.L. Ng, Y. Zhang, C. Owh, F. Wang, Q. Song, T. Feng, B. Zhang, P. Li, X.J. Loh, S.Y. Chan, B.Q.Y. Chan, Progress and opportunities in additive manufacturing of electrically conductive polymer composites, Mater. Today Adv. 17 (2023). https://doi.org/10.1016/j.mtadv.2022.100333.

[14] M.A. Shahid, M.M. Rahman, M.T. Hossain, I. Hossain, M.S. Sheikh, M.S. Rahman, N. Uddin, S.W. Donne, M.I.U. Hoque, Advances in Conductive Polymer-Based Flexible Electronics for

Multifunctional Applications, Journal of Composites Science 9 (2025). https://doi.org/10.3390/jcs9010042.

[15] P. Guruprasad Reddy, A. Barua, T. Laukkanen, B. Mostafiz, T. Tirri, A. Vainio, V. Sharma, Sustainable cross-linked poly(glycerol–co–δ–valerolactone) urethane substrates and multipurpose transparent electrodes for wearable electronics, Chemical Engineering Journal 495 (2024). https://doi.org/10.1016/j.cej.2024.153531.

[16] T. Laukkanen, P.G. Reddy, A. Barua, M. Kumar, K. Kolpakov, T. Tirri, V. Sharma, Sustainable castor oil-derived cross-linked poly(ester-urethane) elastomeric films for stretchable transparent conductive electrodes and heaters, J. Mater. Chem. A Mater. 12 (2024) 33177–33192. https://doi.org/10.1039/d4ta05338a.

[17] S.K. Hwang, S.M. Kang, M. Rethinasabapathy, C. Roh, Y.S. Huh, MXene: An emerging two-dimensional layered material for removal of radioactive pollutants, Chemical Engineering Journal 397 (2020). https://doi.org/10.1016/j.cej.2020.125428.

[18] T. Du, X. Han, X. Yan, J. Shang, Y. Li, J. Song, MXene-Based Flexible Sensors: Materials, Preparation, and Applications, Adv. Mater. Technol. 8 (2023). https://doi.org/10.1002/admt.202202029.

[19] R. Cai, C. Liang, Y. Duan, Z. Zhao, X. Zhang, P. He, J. Yang, W. Lai, J. Wei, L. Tian, Metallic nanoparticle inks for flexible printed electronics, FlexMat 2 (2025) 225–283. https://doi.org/10.1002/flm2.40.

[20] Y. Ding, S. Xiong, L. Sun, Y. Wang, Y. Zhou, Y. Li, J. Peng, K. Fukuda, T. Someya, R. Liu, X. Zhang, Metal nanowire-based transparent electrode for flexible and stretchable optoelectronic devices, Chem. Soc. Rev. 53 (2024) 7784–7827. https://doi.org/10.1039/d4cs00080c.

[21] H. Ha, C. Amicucci, P. Matteini, B. Hwang, Mini review of synthesis strategies of silver nanowires and their applications, Colloids and Interface Science Communications 50 (2022). https://doi.org/10.1016/j.colcom.2022.100663.

[22] S. Lee, C. Wern, S. Yi, Novel Fabrication of Silver-Coated Copper Nanowires with Organic Compound Solution, Materials 15 (2022). https://doi.org/10.3390/ma15031135.

[23] K. Critchley, B.P. Khanal, M.L. Górzny, L. Vigderman, S.D. Evans, E.R. Zubarev, N.A. Kotov, Near-bulk conductivity of gold nanowires as nanoscale interconnects and the role of atomically smooth interface, Advanced Materials 22 (2010) 2338–2342. https://doi.org/10.1002/adma.201000236.

[24] J.L. Wang, M. Hassan, J.W. Liu, S.H. Yu, Nanowire Assemblies for Flexible Electronic Devices: Recent Advances and Perspectives, Advanced Materials 30 (2018). https://doi.org/10.1002/adma.201803430.

[25] B. Sharma, R.M. Singh, A. Kumar, S. Kumar, Diameter-dependent properties of electrodeposited nickel nanowire arrays, Journal of Materials Science: Materials in Electronics 33 (2022) 14323–14333. https://doi.org/10.1007/s10854-022-08358-8.

[26] S. Wang, K. Chen, M. Wang, H. Li, G. Chen, J. Liu, L. Xu, Y. Jian, C. Meng, X. Zheng, S. Liu, C. Yin, Z. Wang, P. Du, S. Qu, C.W. Leung, Controllable synthesis of nickel nanowires and its application in high sensitivity, stretchable strain sensor for body motion sensing, J. Mater. Chem. C Mater. 6 (2018) 4737–4745. https://doi.org/10.1039/c7tc05970a.

[27] C.S. Lewis, L. Wang, H. Liu, J. Han, S.S. Wong, Synthesis, characterization, and formation mechanism of crystalline cu and ni metallic nanowires under ambient, seedless, surfactantless conditions, Cryst. Growth Des. 14 (2014) 3825–3838. https://doi.org/10.1021/cg500324j.

[28] Y. Zhang, J. Guo, D. Xu, Y. Sun, F. Yan, Synthesis of Ultralong Copper Nanowires for High-Performance Flexible Transparent Conductive Electrodes: The Effects of Polyhydric Alcohols, Langmuir 34 (2018) 3884–3893. https://doi.org/10.1021/acs.langmuir.8b00344.

[29] J. Wang, Z. Zhang, S. Wang, R. Zhang, Y. Guo, G. Cheng, Y. Gu, K. Liu, K. Chen, Superstable copper nanowire network electrodes by single-crystal graphene covering and their applications in flexible nanogenerator and light-emitting diode, Nano Energy 71 (2020). https://doi.org/10.1016/j.nanoen.2020.104638.

[30] L. Broere, R. Gogoi, A. Barua, N.G. Mathews, S. Granroth, K. Kolpakov, G. Mohanty, E. Peltola, V. Sharma, Durable copper nanowires for flexible curvature sensors, Chemical Engineering Journal Advances 26 (2026). https://doi.org/10.1016/j.ceja.2026.101111.

[31] J. Koo, S. Kwon, N.R. Kim, K. Shin, H.M. Lee, Ethylenediamine-Enhanced Oxidation Resistivity of a Copper Surface during Water-Based Copper Nanowire Synthesis, Journal of Physical Chemistry C 120 (2016) 3334–3340. https://doi.org/10.1021/acs.jpcc.5b10733.

[32] A.S. Hashimi, R.T. Ginting, S.X. Chin, K.S. Lau, M.A. Nazhif Mohd Nohan, S. Zakaria, C.C. Yap, C.H. Chia, Fast microwave-assisted synthesis of copper nanowires as reusable high-performance transparent conductive electrode, Current Applied Physics 20 (2020) 205–211. https://doi.org/10.1016/j.cap.2019.11.006.

[33] F. Qian, P.C. Lan, T. Olson, C. Zhu, E.B. Duoss, C.M. Spadaccini, T.Y.J. Han, Multiphase separation of copper nanowires, Chemical Communications 52 (2016) 11627–11630. https://doi.org/10.1039/c6cc06228h.

[34] C. Kang, S. Yang, M. Tan, C. Wei, Q. Liu, J. Fang, G. Liu, Purification of Copper Nanowires to Prepare Flexible Transparent Conductive Films with High Performance, ACS Appl. Nano Mater. 1 (2018) 3155–3163. https://doi.org/10.1021/acsanm.8b00326.

[35] Z. Yin, S. Chen, Y. Guan, Q. Ran, Q. Zhang, X. Yan, R. Jin, H. Yu, L. Li, J. Yu, Copper Nanowire Dispersion through an Electrostatic Dispersion Mechanism for High-Performance Flexible Transparent Conducting Films and Optoelectronic Devices, ACS Appl. Mater. Interfaces 11 (2019) 5264–5275. https://doi.org/10.1021/acsami.8b19277.

[36] Z. Niu, F. Cui, Y. Yu, N. Becknell, Y. Sun, G. Khanarian, D. Kim, L. Dou, A. Dehestani, K. Schierle-Arndt, P. Yang, Ultrathin Epitaxial Cu@Au Core-Shell Nanowires for Stable Transparent Conductors, J. Am. Chem. Soc. 139 (2017) 7348–7354. https://doi.org/10.1021/jacs.7b02884.

[37] M. César, D. Gall, H. Guo, Reducing Grain-Boundary Resistivity of Copper Nanowires by Doping, Phys. Rev. Appl. 5 (2016) 054018. https://doi.org/10.1103/PhysRevApplied.5.054018.

[38] C. Hwang, J. An, B.D. Choi, K. Kim, S.W. Jung, K.J. Baeg, M.G. Kim, K.M. Ok, J. Hong, Controlled aqueous synthesis of ultra-long copper nanowires for stretchable transparent conducting electrode, J. Mater. Chem. C Mater. 4 (2016) 1441–1447. https://doi.org/10.1039/c5tc03614c.

[39] N.H. Tran, P. Tran, J.H. Lee, Copper Nanowire-Sealed Titanium Dioxide/Poly(dimethylsiloxane) Electrode with an In-Plane Wavy Structure for a Stretchable Capacitive Strain Sensor, ACS Appl. Nano Mater. 5 (2022) 7150–7160. https://doi.org/10.1021/acsanm.2c00963.

[40] S. Yu, Z. Liu, L. Zhao, B. Gong, High-performance flexible transparent conductive tape based on copper nanowires, Opt. Mater. (Amst). 119 (2021). https://doi.org/10.1016/j.optmat.2021.111301.

[41] Y. Shi, H. Li, L. Chen, X. Huang, Obtaining ultra-long copper nanowires via a hydrothermal process, Sci. Technol. Adv. Mater. 6 (2005) 761–765. https://doi.org/10.1016/j.stam.2005.06.008.

[42] M. Bobinger, J. Mock, P. La Torraca, M. Becherer, P. Lugli, L. Larcher, Tailoring the Aqueous Synthesis and Deposition of Copper Nanowires for Transparent Electrodes and Heaters, Adv. Mater. Interfaces 4 (2017). https://doi.org/10.1002/admi.201700568.

[43] N.P. Simonenko, T.L. Simonenko, Y.R. Topalova, P.Y. Gorobtsov, P. V. Arsenov, E.P. Simonenko, Influence of Hydrothermal Synthesis Conditions on Microstructure Characteristics of Copper Nanowires, Russian Journal of Inorganic Chemistry 70 (2025) 968–978. https://doi.org/10.1134/S0036023625601801.

[44] M.J. Kim, P.F. Flowers, I.E. Stewart, S. Ye, S. Baek, J.J. Kim, B.J. Wiley, Ethylenediamine promotes Cu nanowire growth by inhibiting oxidation of Cu(111), J. Am. Chem. Soc. 139 (2017) 277–284. https://doi.org/10.1021/jacs.6b10653.

[45] Y. Javed, K. Ali, K. Akhtar, Jawaria, M.Irfan. Hussain, G. Ahmad, T. Arif, TEM for Atomic-Scale Study: Fundamental, Instrumentation,and Applications in Nanotechnology, in: S. Sharma (Ed.), Handbook of Materials Characterization, Springer International Publishing, 2018: pp. 147–216. https://doi.org/https://doi.org/10.1007/978-3-319-92955-2_5.

[46] K. Akhtar, S.A. Khan, S.B. Khan, A.M. Asiri, Scanning Electron Microscopy: Principle and Applications in Nanomaterials Characterization, in: S.K. Sharma (Ed.), Handbook of Materials Characterization, Springer International Publishing, Cham, 2018: pp. 113–145. https://doi.org/10.1007/978-3-319-92955-2_4.

[47] J.I. Goldstein, D.E. Newbury, P. Echlin, D.C. Joy, Scanning electron microscopy and x-ray microanalysis, 2nd ed., Plenum Press, New York, 1992.

[48] A. Alyamani, O.M. Lemine, FE-SEM characterization of some nanomaterial, in: V. Kazmiruk (Ed.), Scan. Electron Microsc., InTech, London, 2012.

[49] W. Sun, L. Wang, T. Wu, Y. Pan, G. Liu, Communication—Multi-Layer Boron Nitride Nanosheets as Corrosion-Protective Coating Fillers, J. Electrochem. Soc. 163 (2016) C16–C18. https://doi.org/10.1149/2.0301602jes.

[50] H. Khan, A.S. Yerramilli, A. D'Oliveira, T.L. Alford, D.C. Boffito, G.S. Patience, Experimental methods in chemical engineering: X-ray diffraction spectroscopy— <scp>XRD</scp>, Can. J. Chem. Eng. 98 (2020) 1255–1266. https://doi.org/10.1002/cjce.23747.

[51] W.H. Bragg, W.L. Bragg, eds., X-rays and Crystal Structure, G.Bell, London, 1915.

[52] A. Bijelic, A. Rompel, Polyoxometalates: more than a phasing tool in protein crystallography, ChemTexts 4 (2018). https://doi.org/10.1007/s40828-018-0064-1.

[53] J. Kumar, Photoelectron Spectroscopy: Fundamental Principles and Applications, in: S. Sharma (Ed.), Handbook of Materials Characterization, Springer International Publishing, Cham, 2018: pp. 435–495. https://doi.org/10.1007/978-3-319-92955-2_12.

[54] Nexsa G2 Surface Analysis System datasheet, (2022). https://documents.thermofisher.com/TFS-Assets/MSD/Datasheets/ds0364-nexsa-g2-xps.pdf (accessed March 19, 2026).

[55] S. Hemmati, D.P. Barkley, Parametric Study, Sensitivity Analysis, and Optimization of Polyol Synthesis of Silver Nanowires, ECS Journal of Solid State Science and Technology (2017) 132.

[56] S. Mourdikoudis, M. Menelaou, N. Fiuza-Maneiro, G. Zheng, S. Wei, J. Pérez-Juste, L. Polavarapu, Z. Sofer, Oleic acid/oleylamine ligand pair: a versatile combination in the synthesis of colloidal nanoparticles, Nanoscale Horiz. 7 (2022) 941–1015. https://doi.org/10.1039/d2nh00111j.

[57] Z. Yin, C. Lee, S. Cho, J. Yoo, Y. Piao, Y.S. Kim, Facile synthesis of oxidation-resistant copper nanowires toward solution-processable, flexible, foldable, and free-standing electrodes, Small 10 (2014) 5047–5052. https://doi.org/10.1002/smll.201401276.

[58] A.K. Kar, R. Srivastava, Selective synthesis of Cu-Cu 2 O/C and CuO-Cu 2 O/C catalysts for Pd-free C-C, C-N coupling and oxidation reactions, Inorg. Chem. Front. 6 (2019) 576–589. https://doi.org/10.1039/c8qi01198b.

[59] X. Zha, D. Gong, W. Chen, L. Wu, C. Zhang, Synthesis of Copper Nanowires Using Monoethanolamine and the Application in Transparent Conductive Films, Nanomaterials 15 (2025). https://doi.org/10.3390/nano15090638.

[60] S.A. Hassanzadeh-Tabrizi, Precise calculation of crystallite size of nanomaterials: A review, J. Alloys Compd. 968 (2023) 171914. https://doi.org/10.1016/j.jallcom.2023.171914.

[61] P. Scherrer, Estimation of the Size and Internal Structure of Colloidal Particles by Means of Röntgen. Nachrichten von der Gesellschaft der Wissenschaften zu Göttingen, Nachrichten von Der Gesellschaft Der Wissenschaften Zu Göttingen, Mathematisch-Physikalische Klasse 2 (1918) 98–100.

[62] P. Bellchambers, M. Walker, S. Huband, A. Dirvanauskas, R.A. Hatton, Enhanced Oxidation Stability of Transparent Copper Films Using a Hybrid Organic-Inorganic Nucleation Layer, ChemNanoMat 5 (2019) 619–624. https://doi.org/10.1002/cnma.201800667.

[63] M.C. Biesinger, L.W.M. Lau, A.R. Gerson, R.S.C. Smart, Resolving surface chemical states in XPS analysis of first row transition metals, oxides and hydroxides: Sc, Ti, V, Cu and Zn, Appl. Surf. Sci. 257 (2010) 887–898. https://doi.org/10.1016/j.apsusc.2010.07.086.

[64] S. Ye, I.E. Stewart, Z. Chen, B. Li, A.R. Rathmell, B.J. Wiley, How Copper Nanowires Grow and How to Control Their Properties, Acc. Chem. Res. 49 (2016) 442–451. https://doi.org/10.1021/acs.accounts.5b00506.

[65] J. Zhang, X. Zhu, J. Xu, R. Xu, H. Yang, C. Kan, Comparative Study on Preparation Methods for Transparent Conductive Films Based on Silver Nanowires, Molecules 27 (2022). https://doi.org/10.3390/molecules27248907.

[66] S. Nilsson, J.N. El Berch, D. Albinsson, J. Fritzsche, G. Mpourmpakis, C. Langhammer, The Role of Grain Boundary Sites for the Oxidation of Copper Catalysts during the CO Oxidation Reaction, ACS Nano 17 (2023) 20284–20298. https://doi.org/10.1021/acsnano.3c06282.

[67] R. Wang, H. Ruan, Synthesis of copper nanowires and its application to flexible transparent electrode, J. Alloys Compd. 656 (2016) 936–943. https://doi.org/10.1016/j.jallcom.2015.09.279.

[68] P. Tran, N.H. Tran, J.H. Lee, Highly stretchable electroluminescent device based on copper nanowires electrode, Sci. Rep. 12 (2022). https://doi.org/10.1038/s41598-022-13167-4.

[69] D. Kim, J. Kwon, J. Jung, K. Kim, H. Lee, J. Yeo, S. Hong, S. Han, S.H. Ko, A Transparent and Flexible Capacitive-Force Touch Pad from High-Aspect-Ratio Copper Nanowires with Enhanced Oxidation Resistance for Applications in Wearable Electronics, Small Methods 2 (2018). https://doi.org/10.1002/smtd.201800077.

[70] J.J. Patil, W.H. Chae, A. Trebach, K.J. Carter, E. Lee, T. Sannicolo, J.C. Grossman, Failing Forward: Stability of Transparent Electrodes Based on Metal Nanowire Networks, Advanced Materials 33 (2021). https://doi.org/10.1002/adma.202004356.

[71] Z. Yu, X. Jian, J. Wang, X. Zhang, S. Zhai, Advantages and Research Progress of Polycarbonates in Flexible Electronic Devices, Macromol. Rapid Commun. (2025). https://doi.org/10.1002/marc.202500705.

[72] A.R. Rathmell, S.M. Bergin, Y.L. Hua, Z.Y. Li, B.J. Wiley, The growth mechanism of copper nanowires and their properties in flexible, transparent conducting films, Advanced Materials 22 (2010) 3558–3563. https://doi.org/10.1002/adma.201000775.

[73] T. Wang, R. Wang, Y. Cheng, J. Sun, Quasi in Situ Polymerization to Fabricate Copper Nanowire-Based Stretchable Conductor and Its Applications, ACS Appl. Mater. Interfaces 8 (2016) 9297–9304. https://doi.org/10.1021/acsami.5b11143.

[74] A.R. Rathmell, B.J. Wiley, The synthesis and coating of long, thin copper nanowires to make flexible, transparent conducting films on plastic substrates, Advanced Materials 23 (2011) 4798–4803. https://doi.org/10.1002/adma.201102284.

[75] H.C. Chu, Y.C. Chang, Y. Lin, S.H. Chang, W.C. Chang, G.A. Li, H.Y. Tuan, Spray-Deposited Large-Area Copper Nanowire Transparent Conductive Electrodes and Their Uses for Touch Screen Applications, ACS Appl. Mater. Interfaces 8 (2016) 13009–13017. https://doi.org/10.1021/acsami.6b02652.

[76] Q. Xie, Z. Yan, S. Wang, Y. Wang, L. Mei, F. Qin, R. Jiang, Transparent, Flexible, and Stable Polyethersulfone/Copper-Nanowires/Polyethylene Terephthalate Sandwich-Structured Films for High-Performance Electromagnetic Interference Shielding, Adv. Eng. Mater. 23 (2021). https://doi.org/10.1002/adem.202100283.

[77] A. Barua, R. Gogoi, P.G. Reddy, S. Jolaiy, M. Bodaghi, T. Laukkanen, T. Speck, V. Sariola, V. Sharma, Biomimetic freestanding microfractals for flexible electronics, Npj Flexible Electronics 9 (2025) 10. https://doi.org/10.1038/s41528-025-00381-z.

[78] X. Sun, T. Liu, J. Zhou, L. Yao, S. Liang, M. Zhao, C. Liu, N. Xue, Recent Applications of Different Microstructure Designs in High Performance Tactile Sensors: A Review, IEEE Sens. J. 21 (2021) 10291–10303. https://doi.org/10.1109/JSEN.2021.3061677.

[79] D.J. Griffiths, Introduction to Electrodynamics , 5th ed., Cambridge University Press, 2024.